Advanced Materials Interfaces

www.advmatinterfaces.de

REVIEW OPEN ACCESS

Wafer-Scale Single-Crystal Boron Nitride: Synthesis and Integration in 2D Electronics

Jaewon Wang | Soon-Yong Kwon

Department of Materials Science and Engineering and Graduate School of Semiconductor Materials and Devices Engineering, Ulsan National Institute of Science and Technology (UNIST), Ulsan, Republic of Korea

Correspondence: Soon-Yong Kwon (sykwon@unist.ac.kr)

Received: 29 November 2025 | **Revised:** 13 March 2026 | **Accepted:** 23 March 2026

Keywords: 2D electronics | dielectric integration | (MO)CVD growth | stacking control | wafer-scale hBN

ABSTRACT

Hexagonal boron nitride (hBN) has become a cornerstone dielectric and encapsulation material for next-generation 2D electronics. Its atomically flat surface, wide bandgap, chemical stability, low trap density, and high in-plane thermal conductivity collectively enhance carrier mobility, suppress Coulomb and remote phonon scattering, and enable efficient heat dissipation across a range of 2D devices. Translating these properties into practical technologies demands wafer-scale synthesis of hBN films with precise control over thickness, crystallographic orientation, and stacking sequence, along with integration schemes compatible with semiconductor manufacturing. This Review highlights recent advances in scalable vapor-phase synthesis of hBN, emphasizing self-limiting growth mechanisms and epitaxial strategies that yield single-crystalline and stacking-engineered films. We discuss transfer and direct-integration methods for embedding hBN into 2D architectures and correlate synthesis parameters with device-level metrics. Key challenges and future directions are outlined for establishing hBN as a manufacturable platform for high-performance, wafer-scale 2D electronics.

1 | Introduction

Hexagonal boron nitride (hBN) has emerged as a critical dielectric platform in the advancement of 2D electronics and optoelectronics, where it functions as an insulating substrate, encapsulation layer, and interfacial dielectric for a broad range of 2D semiconductors and metals [1–6]. Unlike conventional 3D insulators, hBN offers an atomically smooth, chemically inert surface free of dangling bonds, with an intrinsic van der Waals (vdW) gap that minimizes interfacial disorder and preserves the intrinsic properties of adjacent 2D layers [3, 7–11]. Its wide bandgap, high in-plane thermal conductivity, and robust resistance to chemical and thermal degradation together enable efficient dielectric screening, suppression of remote phonon scattering, and long-term environmental stability [12–19]. These advantages have led to widespread adoption of hBN in 2D (opto)electronic, photonic, and electrochemical devices, where it serves as a foundational dielectric and encapsulating medium [20–35].

The microscopic origins of these functionalities have been most convincingly demonstrated in model devices utilizing mechanically exfoliated, defect-sparse hBN flakes. In such structures, 2D channels—including graphene and transition metal dichalcogenides (TMDs)—exhibit suppressed impurity scattering, reduced potential fluctuations, and enhanced carrier mobility approaching intrinsic limits [1, 3, 4, 36–39]. However, the exceptional performance of these devices depends on high-purity flakes sourced from bulk crystals, inherently limited in lateral size, thickness control, and scalability. As such, they remain unsuitable for wafer-scale manufacturing. This gap has driven substantial efforts toward developing scalable synthesis techniques that can replicate the structural and

This is an open access article under the terms of the Creative Commons Attribution License, which permits use, distribution and reproduction in any medium, provided the original work is properly cited.

© 2026 The Author(s). *Advanced Materials Interfaces* published by Wiley-VCH GmbH

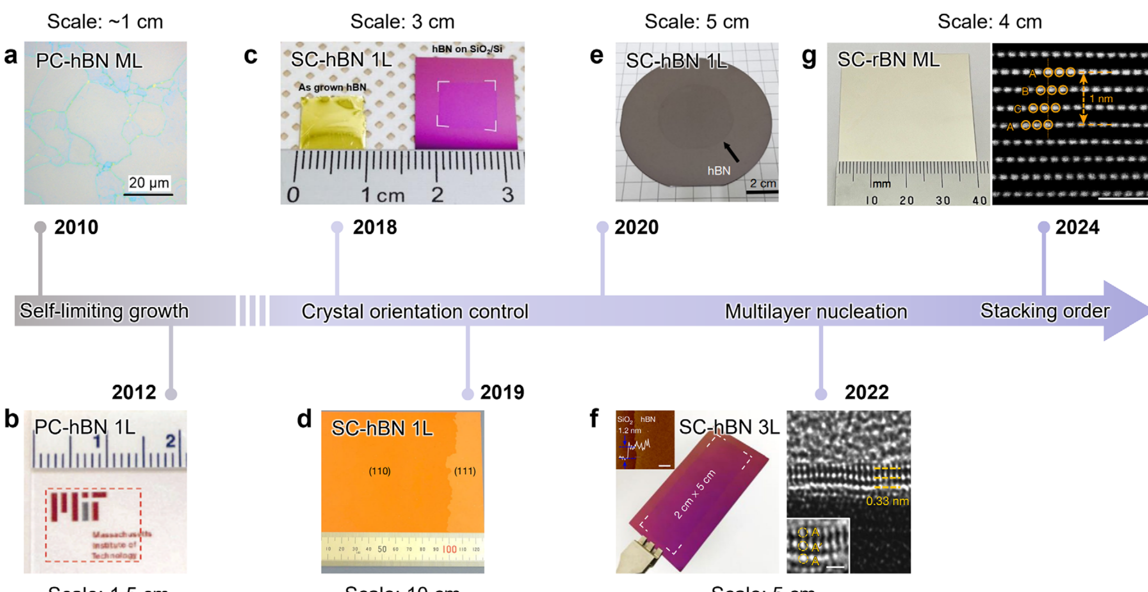

FIGURE 1 | Chronicle timeline of key advancements for wafer-scale BN growth. Four main breakthroughs in wafer-scale BN synthesis are highlighted along the timeline: (i) self-limiting growth achieving polycrystalline (PC) hBN monolayer (1L), (ii) crystal-orientation control enabling wafer-scale SC hBN 1L, (iii) multilayer (ML) nucleation leading to SC hBN tri-layer (3L), and (iv) step-modulation-driven stacking-order control realizing wafer-scale rhombohedral BN (rBN) ML. a) Reproduced with permission [44]. Copyright 2010, American Chemical Society. b) Reproduced with permission [46]. Copyright 2012, American Chemical Society. c) Reproduced with permission [56]. Copyright 2018, American Association for the Advancement of Science. d) Reproduced with permission [49]. Copyright 2019, Springer Nature. e) Reproduced with permission [50]. Copyright 2020, Springer Nature. f) Adapted with permission [51]. Copyright 2022, Springer Nature. g) Adapted with permission [57]. Copyright 2024, Springer Nature.

dielectric quality of exfoliated hBN across technologically relevant areas.

The progressive evolution of wafer-scale hBN growth is schematically summarized in Figure 1. Initial efforts using chemical vapor deposition (CVD) demonstrated the feasibility of growing hBN films over large areas; however, the resulting films typically exhibited polycrystalline morphology, non-uniform thickness, and uncontrolled in-plane orientation [40–48]. More recent studies have exploited the crystallographic symmetry of single-crystal (SC) metal substrates—such as Cu(111), Ni(111), and Cu–Ni(111) alloys—to direct epitaxial alignment of hBN domains, enabling centimeter- to wafer-scale SC growth [28, 49–55]. High-symmetry Cu(111) and Ni(111) surfaces [50–52], along with Cu–Ni (111) alloys [28], have proven particularly effective in suppressing inversion domains and grain boundaries by promoting a well-defined epitaxial relationship between the hBN lattice and the underlying metal.

Building on this monolayer epitaxy, control over nucleation kinetics and precursor supersaturation has recently enabled deterministic multilayer nucleation on such SC templates, leading to wafer-scale SC trilayer (3L) and thicker SC hBN films that preserve in-plane registry [51]. Meanwhile, the growth community has addressed intrinsic limitations of metal foils—including surface roughness, thickness non-uniformity, and thermal expansion mismatch—that often induce wrinkles or folds during cooldown or transfer [50]. These challenges have motivated the development of ultraflat Cu(111) and Cu/Ni(111) wafers compatible with silicon processing flow, offering improved platforms for uniform and scalable hBN growth [28, 50]. Most recently, step-modulated metal surfaces and tailored growth protocols have been employed to break interlayer inversion symmetry, enabling the selective formation of rhombohedral BN (rBN) multilayers [57].

Concurrent with advances in growth, scalable integration techniques have been developed to incorporate as-grown hBN films into 2D electronic architectures. Transfer methods—such as polymer-assisted release [51], electrochemical bubbling [50], and direct growth on insulating or functional substrates [53]—aim to preserve the structural continuity and minimize interfacial contamination of the films. These efforts have enabled not only single-device demonstrations but also the fabrication of statistically meaningful arrays of hBN-based dielectrics in field-effect transistors (FETs), facilitating evaluation of device-to-device variability and reliability at scale.

In this Review, we comprehensively examine how recent advances in scalable hBN synthesis and integration are reshaping the landscape of 2D electronics. We focus on the interplay between growth kinetics, substrate crystallography, and stacking sequence control, and how these factors govern key device parameters such as dielectric screening, phonon scattering, and thermal dissipation. In doing so, we identify persistent bottlenecks—including defect formation during growth, transfer-induced contamination or strain, and incompatibility with back-end-of-line (BEOL) processing—that limit full-scale deployment of hBN in electronics. Lastly, we outline future directions for wafer-scale hBN, including stacking-phase engineering, defect suppression strategies, dry transfer routes, and unified benchmarking metrics that link materials quality to electrical performance.

21967350, 0, Downloaded from https://advanced.onlinelibrary.wiley.com/doi/10.1002/admi.202501079 by Ulsan National Institute Of, Wiley Online Library on [09/04/2026]. See the Terms and Conditions (https://onlinelibrary.wiley.com/terms-and-conditions) on Wiley Online Library for rules of use; OA articles are governed by the applicable Creative Commons License

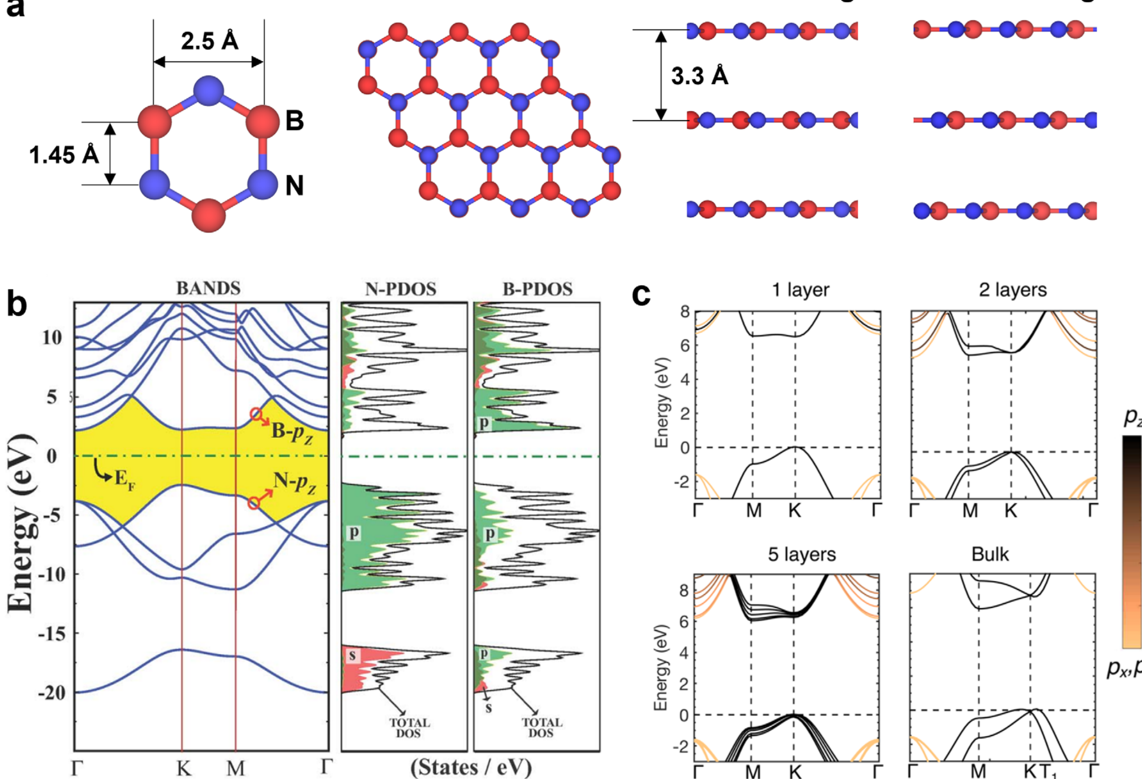

FIGURE 2 | Crystal and electronic structure of layered boron nitride. a) Atomic structure of a BN hexagon and monolayer, and schematic side views of different stacking sequences (AA′ and ABC). b) Representative bulk band structure and projected density of states, highlighting the wide band gap with N-2p_z states dominating the valence-band edge and B-2p_z states the conduction-band edge. Reproduced with permission [58]. Copyright 2009, American Physical Society. c) Evolution of the band dispersion from monolayer to bulk, showing the increasing interlayer coupling of p_z orbitals and the emergence of an indirect gap in multilayer and bulk hBN. Adapted with permission [60]. Copyright 2018, American Chemical Society.

2 | Roles of hBN on 2D Electronics

2.1 | Intrinsic Properties

Layered BN crystallizes in a honeycomb lattice of alternating B and N atoms, where each atom is covalently bonded to three neighbors via sp^2-hybridized B—N bonds (≈1.45 Å) (Figure 2a). Adjacent layers are stacked along the c axis and separated by a vdW gap of ∼3.3 Å, with only weak interlayer interactions compared with the strong in-plane bonds [58–60]. This atomic arrangement, characterized by strong ionicity, results in a wide bandgap of approximately 6 eV (Figure 2b,c). Furthermore, the combination of light constituent atoms and strong B—N bonds leads to low anharmonicity, which support high group velocities and long mean free paths for acoustic phonons along the basal plane [61]. These features give rise to high in-plane thermal conductivity, allowing hBN to function as an efficient heat spreader while maintaining its superior electrical insulation.

Several stacking sequences have been identified for layered BN. The most common bulk phase is usually referred to as hBN with AA′ stacking, in which B atoms in one layer are positioned approximately above N atoms in the neighboring layer and vice versa, leading to a two-layer stacking periodicity. Bernal-type AB stacking can also be stabilized in thin films, where one sublattice is laterally shifted relative to the underlying layer, while rhombohedral BN (rBN) adopts an ABC stacking sequence with a three-layer periodicity [62]. These different registries modify the interlayer symmetry and thus influence both the electronic structure and possible out-of-plane polarization. Recent experimental studies have exploited this polarity to demonstrate ferroelectric-like switching behavior by controlling interlayer sliding or stacking transitions between different polar configurations [63–66]. Such stacking-controlled polarization in rBN has been proposed as a route toward nonvolatile functional dielectrics, including gate insulators with switchable polarization, memory elements, and tunable interfacial fields for adjacent 2D semiconductors.

2.2 | Suitability of hBN as a Dielectric Layer

hBN is intrinsically suited for 2D electronics due to its unique electrostatic properties and atomic-scale surface quality. When used as a substrate, gate dielectric, or encapsulation layer for 2D channels, hBN provides thickness-independent screening that helps to reduce potential fluctuations originating from trapped charges and remote Coulomb perturbations, thereby stabilizing the electrostatic environment of the active material [2, 17]. This stabilizing effect, coupled with the absence of dangling bonds and surface states, allows for the preservation of high carrier mobility in adjacent 2D semiconductors.

21967350, 0, Downloaded from https://advanced.onlinelibrary.wiley.com/doi/10.1002/admi.202501079 by Ulsan National Institute Of, Wiley Online Library on [09/04/2026]. See the Terms and Conditions (https://onlinelibrary.wiley.com/terms-and-conditions) on Wiley Online Library for rules of use; OA articles are governed by the applicable Creative Commons License

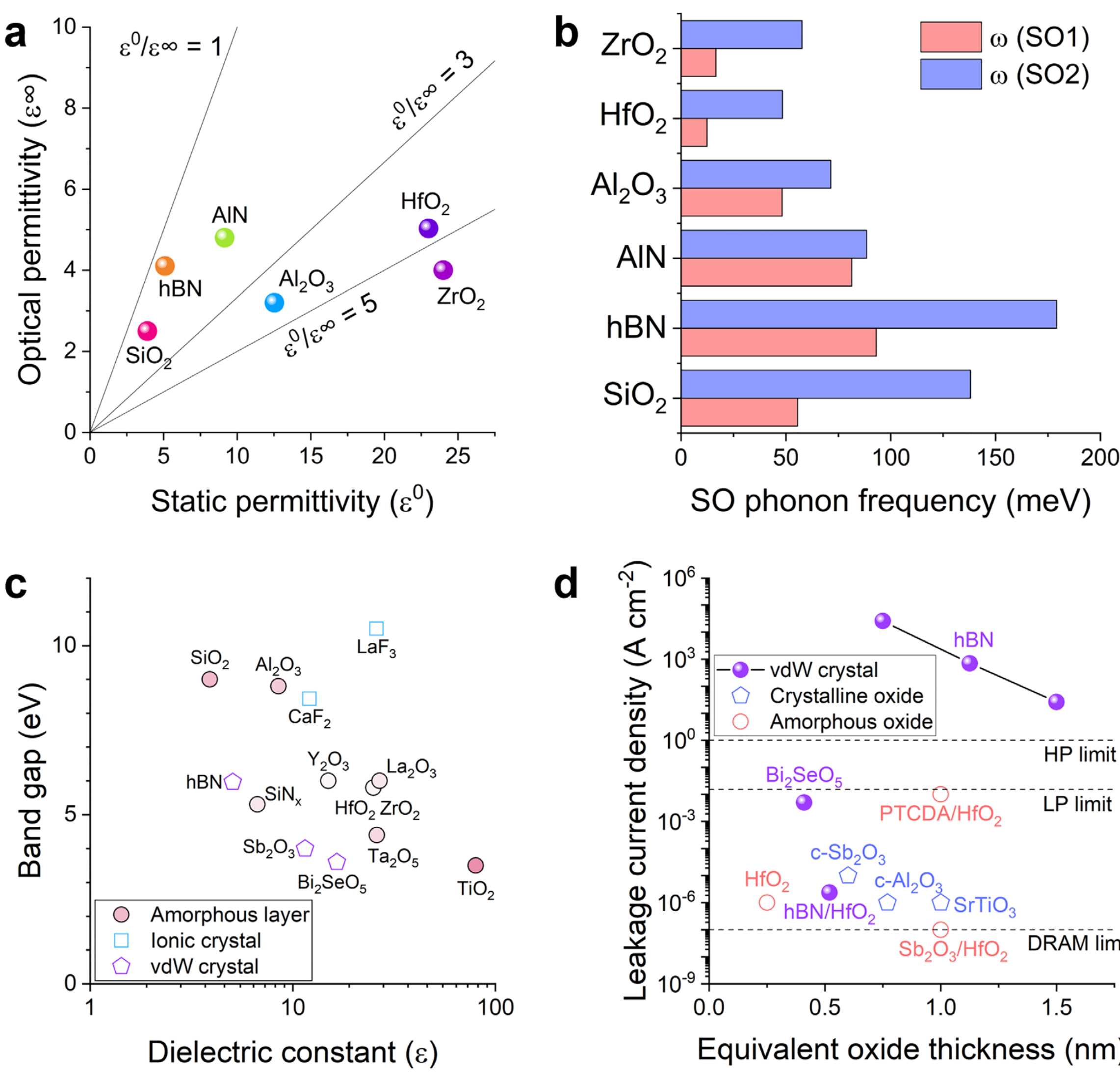

FIGURE 3 | Limitations of hBN as dielectric layer for 2D system. a,b) Comparison of dielectric properties (Refs. [69, 70]). a) Relationship between static and optical permittivity for common dielectrics. b) Surface optical (SO) phonon frequency of various dielectrics. c) Relationship between band gap and dielectric constant (ε) for various gate insulators, categorized by materials class: amorphous layers, ionic crystals, and van der Waals (vdW) crystals [71–77]. d) Comparative analysis of leakage current density as a function of equivalent oxide thickness (EOT) [28, 78–85]. The low-power and high-performance limits are donated as LP and HP, respectively.

The primary advantage of hBN in enhancing device performance lies in its ability to mitigate scattering. Charge transport in 2D semiconductors is strongly influenced by the surrounding dielectric environment [67, 68]. While high-κ dielectrics are effective for scaling, they typically induce significant remote phonon scattering due to their low surface optical (SO) phonon frequencies and large disparities between static and optical permittivity (Figure 3a,b) [69, 70]. In contrast, hBN features significantly higher SO phonon energies and moderate permittivity, which results in much weaker coupling to remote polar modes. By suppressing these extrinsic scattering sources, hBN encapsulation allows 2D channels to more closely approach their intrinsic phonon-limited mobility.

Despite these advantages, the use of hBN as a standalone gate dielectric faces challenges during aggressive device scaling. As illustrated in Figure 3c, hBN possesses a relatively low intrinsic dielectric constant (~5) compared to high-κ dielectrics. This lower permittivity limits the gate capacitance and hinders the reduction of equivalent oxide thickness (EOT). Comparative analysis of leakage current density as a function of EOT (Figure 3d) reveals that standalone hBN layers tend to exceed the high-performance (HP) limit when the EOT is scaled below 2 nm. Consequently, hBN alone may not satisfy the leakage requirements necessary for scaled 2D transistors.

To address these limitations, recent studies have increasingly focused on utilizing synthesized SC hBN films as an interfacial dielectric layer. In particular, research on gate scaling using hybrid stacks of hBN and HfO_2 has demonstrated superior performance by combining clean interface of hBN with the high capacitance of the oxide [28]. Notably, such hybrid dielectrics have achieved a leakage current density of approximately 10^{-6} A cm^{-2} at an EOT of 0.5 nm, successfully meeting the benchmarks set by IRDS 2028. This approach effectively leverages hBN to suppress interfacial scattering while utilizing industrial high-κ

21967350, 0, Downloaded from https://advanced.onlinelibrary.wiley.com/doi/10.1002/admi.202501079 by Ulsan National Institute Of, Wiley Online Library on [09/04/2026]. See the Terms and Conditions (https://onlinelibrary.wiley.com/terms-and-conditions) on Wiley Online Library for rules of use; OA articles are governed by the applicable Creative Commons License

dielectrics to achieve the necessary gate scaling, presenting a viable path for the next generation of 2D material-based electronic systems.

3 | Approaches for Scalable Synthesis of BN Films

Advances in the wafer-scale synthesis of 2D materials are increasingly driven by the necessity for integration with existing semiconductor manufacturing lines, which typically utilize 100–300 mm wafers and standardized front-end processes [86–89]. This drive has shifted the focus of 2D electronics from small, exfoliated flakes toward continuous, thickness-controlled, and ultimately SC layers grown directly on wafer platforms. However, the wafer-scale synthesis of SC hBN remains less mature compared to other 2D materials. Unlike TMDs, which can be grown directly on insulating wafers such as Si or sapphire with high crystallinity, most large-area hBN growth studies necessitate high thermal budgets and the use of metal layers to guide crystal orientation.

Furthermore, growth on catalytic metal substrates presents unique challenges; unlike insulating wafers (e.g., sapphire) that do not react with precursors during the growth, the growth mechanism and morphologies of hBN on metal surfaces vary significantly depending on the growth temperature, pressure, and precursor species. Consequently, optimizing growth parameters to achieve uniform, wafer-scale, SC hBN films remains a formidable task. Section 3 summarizes the growth parameters optimized to enhance crystallinity during the large-area synthesis of hBN, with a particular focus on the distinct growth behaviors observed on different substrates, and outlines the key growth mechanisms involved.

3.1 | Precursors for hBN Growth

In the early stages of hBN synthesis, sapphire was the most widely utilized substrate via metal-organic chemical vapor deposition using B precursors such as triethylboron (TEB) or diborane (B_2H_6), with NH_3 serving as the standard N precursor [41, 43, 90]. To overcome the low chemical reactivity of NH_3, growth was typically conducted at high temperatures exceeding 1400°C. However, these high-temperature sapphire-based processes faced significant challenges in controlling nucleation and lateral growth due to the disparity in reactivity between the boron and nitrogen sources. As a result, the synthesized films often exhibited small grain sizes and were frequently characterized as turbostratic BN (t-BN) rather than phase-pure hBN [42].

To address these limitations, research efforts shifted toward more efficient precursors and catalytic platforms. Researchers began adopting single-source precursors—such as ammonia borane and borazine—where B–N bonds are pre-established, and transitioned to catalytic metal substrates [44, 91]. The use of metal substrates significantly lowered the required thermal budget and provided a template to guide the crystal orientation of the hBN domains [45]. Since 2010, this shift has enabled the synthesis of large-area, high-quality hBN films that can be successfully transferred to target substrates for electrical and structural characterization. Representative studies that have demonstrated wafer-scale hBN synthesis, along with their respective substrates, precursors, and growth temperatures, are summarized in Table 1.

3.2 | Substrates for hBN Growth

The synthesis of scalable hBN is highly dependent on the choice of substrate, which modulates the growth kinetics through its specific metal species, surface orientation, and structural support. In the range of typical growth temperatures ($T > 1000°C$), the solubility of B and N varies significantly depending on the metal species. Cu exhibits low solubility for both B and N, which, when combined with optimized precursor vapor pressure, facilitates the growth of hBN monolayer. In contrast, metals such as Ni and Fe, as well as their respective alloys, possess higher solubility for B and N, making them more suitable for the synthesis of Multilayer hBN films.

Beyond the specific metal species, the crystallographic orientation of the substrate surface dictates the preferred orientation of the grown hBN domains. On polycrystalline surfaces, hBN domains often fail to stitch seamlessly at metal grain boundaries, leading to structural defects and discontinuities. Therefore, achieving unidirectional alignment of BN crystal along the growth substrate is essential for high-quality synthesis. Recent studies have demonstrated that annealing various metal foils can yield specific orientations, such as (111), (100), and (520), enabling the growth of SC hBN films. A more detailed discussion on the specific strategies for SC growth will be provided in Section 4.

Despite the progress in controlling substrate orientation, the use of metal foils presents inherent limitations. The intrinsic surface roughness of foils prevents the formation of atomically flat hBN, and strain associated with high-step edges often causes folding and wrinkles after the transfer process. Furthermore, foil-based synthesis is difficult to integrate into standardized semiconductor manufacturing lines. To address these issues, recent research has pivoted toward the use of SC metal films grown on supporting wafers, such as sapphire. This approach allows for the acquisition of atomically flat hBN films compatible with wafer-scale processes. However, challenges remain, including the difference in thermal expansion coefficients between the metal film and the sapphire substrate, as well as the restricted range of available crystal orientations.

3.3 | Growth Kinetics of hBN

The growth behavior on metals can be rationalized by three limiting kinetic regimes, illustrated in Figure 4. In the surface-reaction regime, precursor molecules decompose and incorporate directly at the metal surface, with negligible dissolution of B and N into the bulk [48]. The hBN thickness is then mainly determined by surface reaction rates and precursor supply, allowing quasi–layer-by-layer growth and better thickness control. Importantly, even when employing substrates and precursors that follow this surface-mediated mechanism, maintaining an appropriate precursor partial pressure during growth is critical; excessive precursor injection can lead to a loss of nucleation control, resulting in entirely different growth morphologies [100]. Furthermore, under conditions of sufficiently controlled

21967350, 0, Downloaded from https://advanced.onlinelibrary.wiley.com/doi/10.1002/admi.202501079 by Ulsan National Institute Of, Wiley Online Library on [09/04/2026]. See the Terms and Conditions (https://onlinelibrary.wiley.com/terms-and-conditions) on Wiley Online Library for rules of use; OA articles are governed by the applicable Creative Commons License

TABLE 1 | Summary of scalable hBN growth on various substrates. Growth temperatures are denoted as *T*. The crystallinity is specified only for single-crystal (SC) structures, and the layer thickness is categorized into monolayer (1L), multilayer (ML) with thicknesses in the nanometer range and bulk film with thickness over 1 µm. Notably, this summary specifically selects representative studies that provide visual evidence of transferred hBN films onto target substrates.

Type	Substrate	Precursors	*T* (°C)	Growth scale	Properties	Refs.
Insulating wafer (non-catalytic)	c-plane sapphire	Ammonia borane	1400	2-inch	ML	[92]
	a-plane sapphire	B_2H_6, NH_3	1300	—	ML	[93]
	m-plane sapphire	Ion beam sputtering (B target, N_2/Ar gas)	1000	2-inch	m-plane hBN, ML	[94]
	Ge (110)	Borazine	920	—	1L	[95]
Catalytic metal foil	Au/W foil	Borazine	1100	3 cm × 3 cm	SC, 1L	[56]
	Cu foil	Ammonia borane	1000	—	1L	[46]
	Ni foil	B_2H_6, NH_3	1025	—	ML	[45]
	Fe foil	Borazine	1100	3 cm × 3 cm	ML	[96]
	Pt foil	Borazine	1100	5 cm × 2 cm	1L	[48]
	Cu (110) foil	Ammonia borane	1035	10 cm × 10 cm	SC, 1L	[49]
	Cu (111) foil	Ammonia borane	1050	7 cm × 2.5 cm	SC, 1L	[55]
	Ni (111) foil	Borazine	1220	5 cm × 2 cm	SC, hBN, 3L	[51]
	FeNi (111) foil	Hot-pressed BN paper	1250	2 cm × 1 cm	SC, rBN, bulk film (>1 µm)	[97]
	Ni (520) foil	Ammonia borane	1350, 1410	4 cm × 4 cm	SC, rBN, ML	[57]
Metal film supported on wafer	Fe–Ni (111) film/sapphire	Ammonia borane	1050	—	ML	[98]
	Fe–Ni (111) film on $MgAl_2O_4$	Borazine	1100	—	ML	[99]
	Cu (111) film/sapphire	Ammonia borane	1050	2-inch	SC, 1L	[50]
	$Cu_{0.8}Ni_{0.2}$ (111) film/sapphire	Ammonia borane	1000	4-inch	SC, 1L	[28]
	Ni(111)/sapphire	triethyl-boron (TEB), NH_3	1100	2-inch	SC, 2L	[52]

precursor partial pressure and low metal substrate solubility, an increase in growth time does not lead to an increase in the number of hBN layers in the surface-reaction regime, which facilitates a self-limiting growth behavior.

In contrast, the surface-segregation and dissolution–precipitation regimes are generally preferred for substrates with high solubility for B or N, such as Ni and Fe, rather than Cu. In the surface-segregation regime, B and N dissolve into the near-surface region of an alloy during high-temperature exposure and subsequently segregate back to the surface during cooling, forming BN layers whose thickness depends on the solubility and cooling rate [99]. In the dissolution–precipitation regime, substantial amounts of B and N dissolve into the bulk metal at high temperature and later precipitate at steps and grain boundaries as the substrate cools, leading to multilayer or rhombohedral BN with thickness variations tied to diffusion paths [97]. Unlike the surface-reaction pathway, the number of grown layers in these solubility-driven regimes tends to increase not only with extended growth times but also with slower cooling rates, which often produces nonuniform multilayers or mixed stacking. For applications that require deterministic monolayer or few-layer hBN, growth conditions and catalyst designs that favor the surface-reaction pathway, while minimizing bulk dissolution and segregation, are therefore considered most suitable.

3.4 | Self-Limiting Growth of hBN

Precise thickness control is essential for integrating hBN into 2D electronics, because dielectric strength, tunnelling resistance, and screening properties are all strongly layer dependent. Rather than relying on ex situ etching or growth-time calibration, many recent studies have sought to engineer a self-limiting regime in which the growth rate naturally decays to zero after formation of a monolayer or well-defined few-layer film. Figure 5 summarizes several representative strategies to realize such self-limiting behavior in both CVD and MOCVD processes.

In catalytic CVD using borazine on Cu, self-limiting growth can be obtained by carefully tuning the precursor partial pressure [100]. At low to moderate borazine pressures, the hBN thickness increases only during an initial transient and then saturates at approximately one monolayer, even when the growth time is extended, indicating that the catalytic surface becomes effectively passivated once a closed hBN sheet is formed (Figure 5a). At

21967350, 0, Downloaded from https://advanced.onlinelibrary.wiley.com/doi/10.1002/admi.202501079 by Ulsan National Institute Of, Wiley Online Library on [09/04/2026]. See the Terms and Conditions (https://onlinelibrary.wiley.com/terms-and-conditions) on Wiley Online Library for rules of use; OA articles are governed by the applicable Creative Commons License

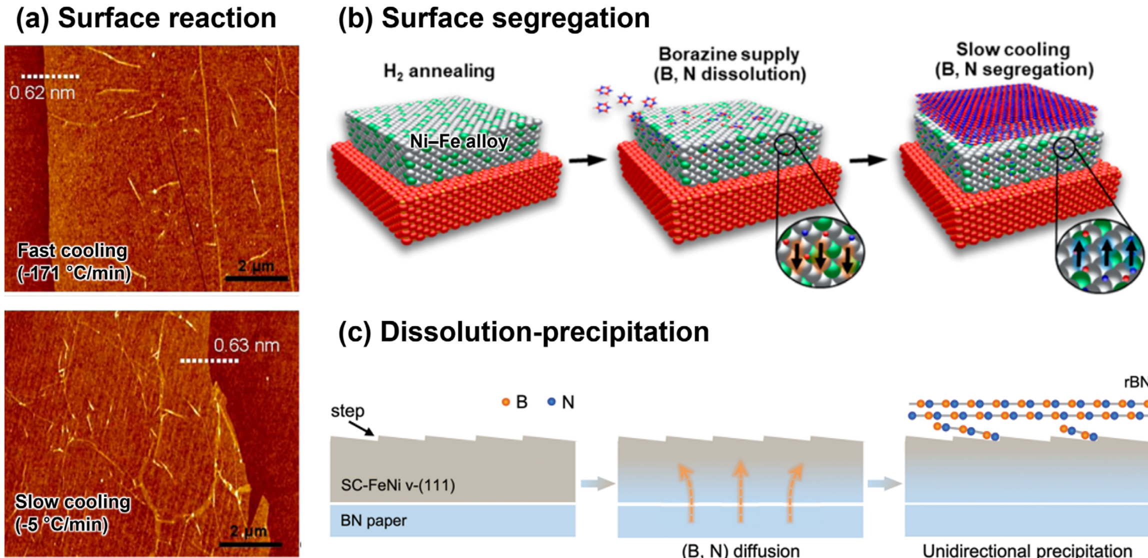

FIGURE 4 | Growth kinetics on metal substrates. a) Surface reaction: AFM images of hBN transferred on SiO_2/Si substrates under fast and slow cooling. Adapted with permission [48]. Copyright 2014, American Chemical Society. b) Surface segregation: schematic of H_2 annealing, borazine exposure with B and N dissolving into the near-surface alloy, and their segregation back to the surface during slow cooling to form hBN. Adapted with permission [99]. Copyright 2018, American Chemical Society. c) Dissolution–precipitation: schematic of B, N diffusion from the bulk of a stepped SC Fe–Ni substrate and unidirectional precipitation along vicinal steps, yielding rhombohedral BN. Adapted with permission [97]. Copyright 2023, John Wiley and Sons.

higher borazine pressures, however, the surface is oversupplied with B–N species, secondary nucleation occurs on top of the first layer, and the thickness increases roughly linearly with time, so that self-limitation is lost. This establishes a finite processing window in which the precursor flux is sufficient to close the first layer but insufficient to sustain multilayer nucleation.

A complementary approach exploits the high solubility of B and N in Fe foils [101]. When the substrate is pre-annealed in hydrogen, B and N can dissolve and later segregate back to the surface during growth, driving the formation of nonuniform multilayer hBN. In contrast, pre-annealing in NH_3 fills near-surface sites with nitrogen and modifies the local chemical potential, thereby promoting monolayer formation by confining nucleation to a single surface layer and suppressing subsequent multilayer growth (Figure 5b).

In MOCVD, where triethylboron (TEB) and NH_3 are used as B and N precursors, self-limiting growth has been achieved by operating under strongly N-rich conditions [102]. As the NH_3/TEB ratio is increased, the measured deposition rate decreases with NH_3 flow and partial pressure, reflecting a transition to a reaction-limited regime in which competitive adsorption and desorption of N-containing species reduce the effective B–N incorporation rate (Figure 5c). Within this high-N/B window, local variations in precursor partial pressure along the wafer lead to minimal changes in thickness, and the film naturally converges toward a monolayer or few-layer state. Collectively, these examples demonstrate that self-limiting hBN growth can be engineered either by passivating the catalytic surface, by controlling subsurface solubility reservoirs, or by slowing the surface reaction kinetics through an excess of N.

4 | SC hBN Growth

4.1 | Origins for SC Growth

Preferred orientations of hBN on crystalline metal substrates have been analyzed in detail to understand how epitaxy can be exploited for SC growth. Because the hBN lattice has three-fold rotational symmetry, triangular domains on high-symmetry metal surfaces often appear in antiparallel pairs rotated by 60°, which merge into polycrystalline films with twin boundaries. Recent theoretical work has shown that the alignment of hBN on transition-metal surfaces is governed by the registry between the zigzag directions of the BN network and high-symmetry directions of the substrate, together with the detailed interaction of hBN edges with atomic step edges [103, 104]. In this regard, it has been confirmed across a wide range of SC metal substrates and growth mechanisms that SC hBN growth is consistently facilitated through this step-guided growth approach (Table 2).

DFT calculations of zigzag hBN edges on low-index Cu surfaces provide a useful framework for rationalizing these preferred orientations (Figure 6a). The binding energy as a function of the in-plane angle between the hBN zigzag direction and substrate close-packed directions exhibits periodic minima that reflect the symmetry of each facet: on Cu(111) the energy profile repeats every 60°, on Cu(100) every 90°, and on Cu(110) every 120° [104]. These results indicate that on the (110) surface a single crystallographic orientation is energetically favored within one 120° sector, whereas on the (111) surface two nearly degenerate orientations related by a 60° rotation are expected. The latter degeneracy naturally leads to antiparallel domains and makes mono-orientation

21967350, 0, Downloaded from https://advanced.onlinelibrary.wiley.com/doi/10.1002/admi.202501079 by Ulsan National Institute Of, Wiley Online Library on [09/04/2026]. See the Terms and Conditions (https://onlinelibrary.wiley.com/terms-and-conditions) on Wiley Online Library for rules of use; OA articles are governed by the applicable Creative Commons License

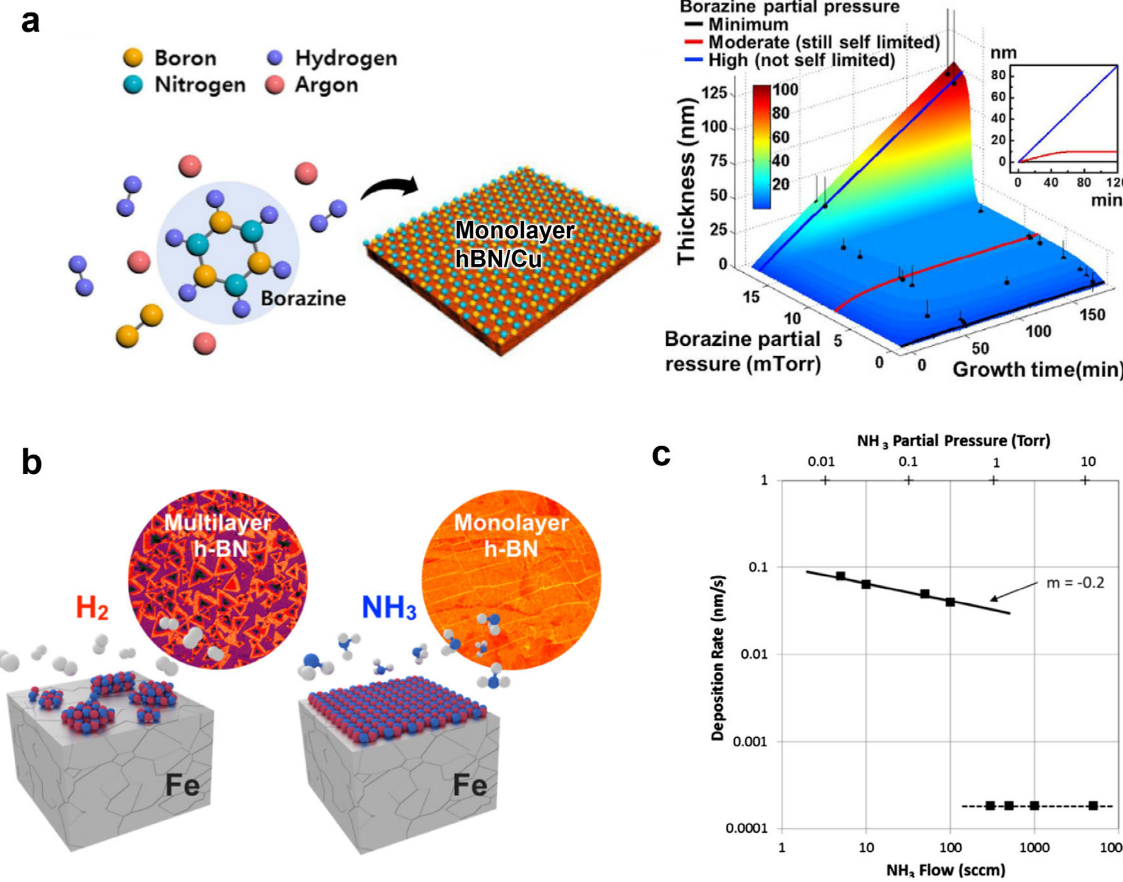

FIGURE 5 | Approaches for self-limiting growth. a) Borazine partial-pressure control on Cu: self-limiting monolayer CVD window as a function of borazine partial pressure and growth time. Adapted under the terms of the CC-BY 4.0 license (http://creativecommons.org/licenses/by/4.0/) [100]. Copyright 2016, The Authors, Published by Springer Nature. b) NH_3 pre-annealing of Fe foils: self-limiting monolayer nucleation enabled by a subsurface nitrogen reservoir, in contrast to multilayer growth after H_2 annealing. Reproduced under the terms of the CC-BY 4.0 license (http://creativecommons.org/licenses/by/4.0/) [101]. Copyright 2016, The Authors, Published by American Chemical Society. c) N-rich MOCVD condition (high NH_3/TEB ratio): reaction-limited regime with decreasing deposition rate that supports self-limiting hBN deposition. Reproduced with permission [102]. Copyright 2018, Elsevier.

TABLE 2 | Summary of hBN growth under various metal substrates and their corresponding growth mechanisms. This table summarizes representative studies focusing exclusively on the wafer-scale SC growth of hBN.

Substrate	Layer/thickness	Phase	Growth mechanism	Refs.
Cu (110) foil	1L	Hexagonal	Self-limiting growth	[49]
Cu (111) foil		Hexagonal		[55]
Cu (111) film/sapphire		Hexagonal		[50]
$Cu_{0.8}Ni_{0.2}$ (111) film/sapphire		Hexagonal		[28]
Ni (111)/sapphire	2L	Hexagonal	Self-limiting growth	[52]
Ni (111) foil	2–5L	Hexagonal	Multilayer nucleation	[51]
Ni (520) foil	2.2–12 nm	Rhombohedral	Layer-by-layer growth	[57]
FeNi (111) foil	Bulk (>1 µm)	Rhombohedral	Dissolution-precipitation	[97]

21967350, 0, Downloaded from https://advanced.onlinelibrary.wiley.com/doi/10.1002/admi.202501079 by Ulsan National Institute Of, Wiley Online Library on [09/04/2026]. See the Terms and Conditions (https://onlinelibrary.wiley.com/terms-and-conditions) on Wiley Online Library for rules of use; OA articles are governed by the applicable Creative Commons License

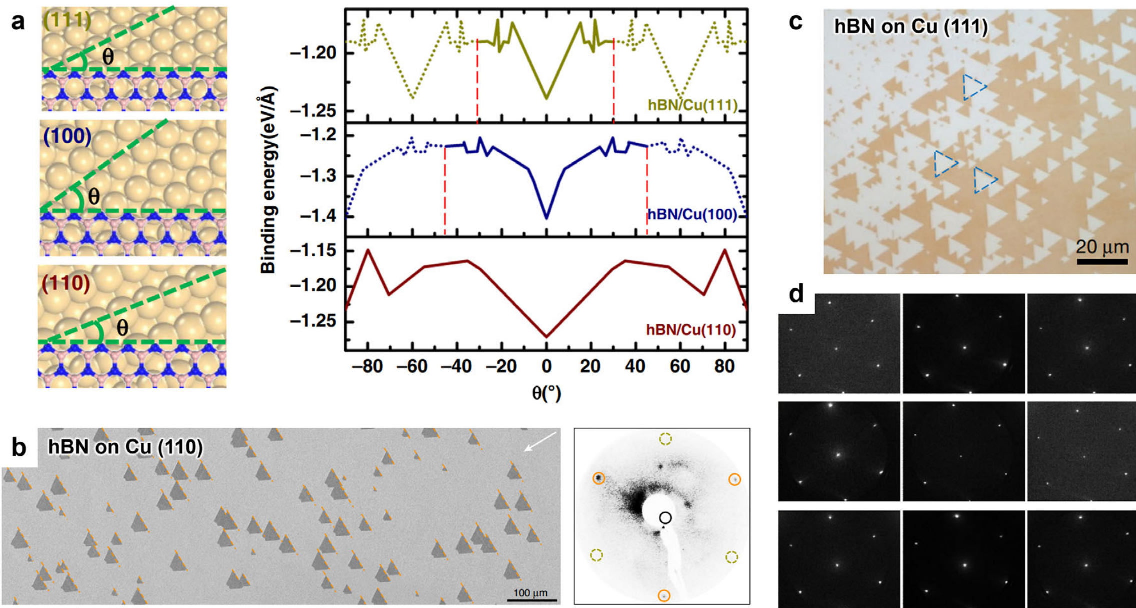

FIGURE 6 | Preferred orientations of hBN on metal substrates. a) DFT-calculated binding energy of hBN edges as a function of in-plane rotation angle on Cu(111), Cu(100), and Cu(110), showing symmetry-dependent preferred orientations. Adapted under the terms of the CC-BY 4.0 license (http://creativecommons.org/licenses/by/4.0/) [104]. Copyright 2020, The Authors, Published by Springer Nature. b) Step-guided unidirectional hBN domains on Cu(110): SEM image of aligned triangular domains and corresponding LEED pattern with one set of diffraction spots. Adapted with permission [49]. Copyright 2019, Springer Nature. c,d) SC hBN growth on Cu(111). Adapted with permission [50]. Copyright 2020, Springer Nature. c) Triangular hBN islands on Cu(111) exhibiting two antiparallel orientations related by 60° rotation. d) Micro-LEED patterns from different locations on hBN/Cu(111).

difficult unless additional symmetry-breaking factors are introduced.

Building on this understanding, SC hBN films have been realized on vicinal Cu(110) foils [49]. A low-symmetry Cu(110) surface with parallel <211> step edges is prepared by high-temperature annealing of industrial Cu foils, yielding a 10 × 10 cm^2 SC substrate. During CVD from ammonia borane feedstock, triangular hBN islands nucleate preferentially at these step edges, with their zigzag edges docked along the step direction. Edge–step coupling lifts the 120° periodic degeneracy predicted for a perfectly flat (110) terrace and selects a single in-plane orientation for essentially all nuclei. As growth proceeds, the coalesced film maintains crystallographic continuity across centimetre scales, as confirmed by low-energy electron diffraction (LEED) patterns that show a single set of hBN spots aligned with the underlying Cu lattice over many probed positions (Figure 6b).

SC represents a well-stitched lattice where merge unidirectionally aligned domains coalesce without forming stacking faults. To confirm the absence of grain boundaries (GBs) in the synthesized SC hBN films, researchers have utilized etching processes involving H_2 or UV oxidation and examined the crystal orientation of adjacent domains at atomic resolution [49]. These analyses verified that the domains were seamlessly stitched, maintaining crystallographic continuity without GB formation. Furthermore, as defects like grain boundaries lead to a reduction in the second-harmonic generation (SHG) signal, SHG mapping has emerged as an effective tool for scanning GBs. Recently, this technique has been widely applied to analyze the SC quality and stacking order of various BN films [57].

A complementary strategy has enabled wafer-scale SC hBN growth on Cu(111) thin films supported by c-plane sapphire wafers [50]. In this case, plane-to-plane DFT calculations for small BN clusters on an ideal Cu(111) terrace indicate that two registries, related by a 60° in-plane rotation, have almost identical binding energies, consistent with the formation of antiparallel domains on twinned Cu(111) grains. However, when the Cu(111) film is annealed to remove in-plane twins and to generate uniform atomic steps, the local interaction between hBN nuclei and step edges breaks this degeneracy and selects a unique docking configuration. Under these conditions, triangular monolayer hBN flakes on untwinned Cu(111) all share the same orientation and merge into a continuous film across a two-inch wafer. Micro-spot LEED measurements at tens of sites reveal identical diffraction patterns and scanning tunnelling microscopy images show a uniform hBN lattice without detectable grain boundaries, establishing that the film is SC over the entire wafer (Figure 6c,d).

Together, these studies illustrate a general principle for orientation control of hBN on metal substrates: the combination of facet symmetry, edge binding on terraces, and step-edge docking determines a small set of energetically favored orientations, and appropriately engineered vicinal surfaces can reduce this set to a single orientation. The approach has been extended to other face-centered cubic and related metal surfaces, indicating that step-mediated epitaxy is a broadly applicable route toward wafer-scale SC hBN and, more generally, toward oriented growth of non-centrosymmetric 2D materials.

21967350, 0, Downloaded from https://advanced.onlinelibrary.wiley.com/doi/10.1002/admi.202501079 by Ulsan National Institute Of, Wiley Online Library on [09/04/2026]. See the Terms and Conditions (https://onlinelibrary.wiley.com/terms-and-conditions) on Wiley Online Library for rules of use; OA articles are governed by the applicable Creative Commons License

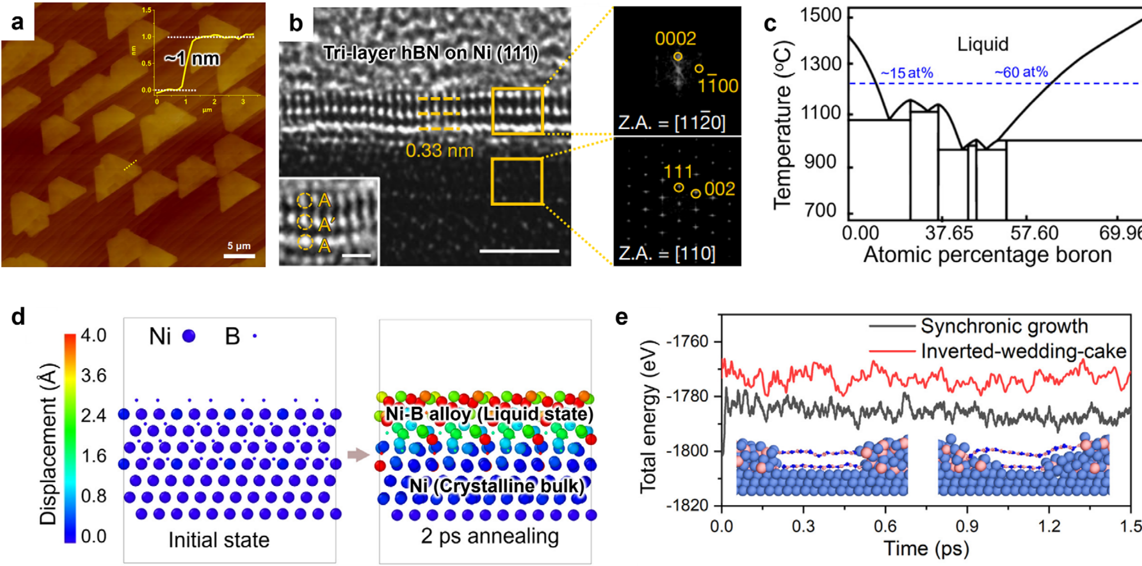

FIGURE 7 | Uniform multilayer hBN growth. a,b) Tri-layer SC hBN on Ni(111): AFM image and height profile (a), and cross-sectional STEM with diffraction patterns (b) confirming three uniformly stacked hBN layers with ~0.33 nm interlayer spacing. a,b) Adapted with permission [51]. Copyright 2022, Springer Nature. c–e) Ni–B surface–liquid–assisted growth mechanism: Ni–B phase diagram indicating a surface-liquid regime at the growth temperature (c); ab initio molecular dynamics snapshots showing formation of a Ni–B liquid layer on crystalline Ni (d); total-energy evolution comparing synchronic multilayer growth with an inverted-wedding-cake mode, demonstrating the energetic stabilization of synchronic multilayer nucleation on the Ni–B liquid surface (e). c–e) Adapted with permission [105]. Copyright 2023, Elsevier.

4.2 | Uniform Multilayer Growth

In many of the electronic devices discussed above, SC hBN monolayer already improves carrier mobility and dielectric stability, but its ultrathin thickness limits gate-field screening, leakage suppression, and control of interlayer tunnelling [51]. For applications such as tunnelling barriers or encapsulation layers in strongly driven devices, there is therefore strong motivation to develop wafer-scale, SC multilayer hBN with well-defined thickness. Most epitaxial growth studies on catalytic metals or insulating wafers, however, have deliberately operated in a self-limiting regime to avoid uncontrolled secondary nucleation, so that the resulting films are predominantly monolayers. Achieving uniform multilayer crystals thus requires a distinct growth mode from the conventional self-limiting monolayer chemistry.

Recent work on Ni(111) has demonstrated that such multilayer SC can be realized when growth proceeds via synchronized multilayer nucleation rather than successive layer-by-layer overgrowth (Figure 7a,b). hBN islands grown on Ni(111) display 1-nm-thick height in AFM, and cross-sectional transmission electron microscopy (TEM) confirms a uniform trilayer thickness across each island [51]. Instead of the “wedding-cake” morphology characteristic of sequential adlayer nucleation, all layers in a given island share nearly identical lateral size and shape, indicating that the number of layers is fixed at the nucleation stage and that the edges of each layer advance together during subsequent growth. Furthermore, the layer thickness can be tuned by modulating the growth environment: increasing the N_2 flow ratio in the carrier gas stabilizes the chemical potential to favor 5-layer nucleation, while reducing the precursor injection rate and higher H_2 flow ratio promotes 2-layer nucleation. However, a significant challenge remains in that the formation energy differences between these multilayer configurations are negligible, making precise and deterministic control over the exact number of layers difficult to achieve.

Follow-up theoretical and computational studies have attributed this unusual behavior to the formation of a liquid Ni–B–rich surface layer at the hBN growth temperature [105]. According to thermodynamic analysis and ab initio molecular dynamics, when the boron content in the near-surface region exceeds the solid–liquid boundary in the Ni–B phase diagram, a thin molten alloy film develops on top of the crystalline Ni(111) substrate (Figure 7c,d). hBN multilayers are then stabilized at the interface between this disordered Ni–B layer and the underlying solid Ni. The liquid layer simultaneously passivates the reactive edges of all hBN layers, preventing their coalescence into a tapered stack, and serves as a reservoir of B–N species that feed each layer at comparable rates. Under these conditions, the energetics favor a synchronic configuration in which all layers grow laterally at nearly the same speed (Figure 7e), resulting in wafer-scale SC multilayer hBN films with a uniform, thickness-defined dielectric platform for 2D electronics.

4.3 | Strategies for Stacking-Sequence Modulation

In layered BN, the AA′ stacking sequence of hexagonal BN is normally the thermodynamically favored configuration, because each B atom tends to sit above an N atom in the adjacent layer and vice versa, restoring inversion symmetry and minimizing the interlayer energy. This strong energetic

21967350, 0, Downloaded from https://advanced.onlinelibrary.wiley.com/doi/10.1002/admi.202501079 by Ulsan National Institute Of, Wiley Online Library on [09/04/2026]. See the Terms and Conditions (https://onlinelibrary.wiley.com/terms-and-conditions) on Wiley Online Library for rules of use; OA articles are governed by the applicable Creative Commons License

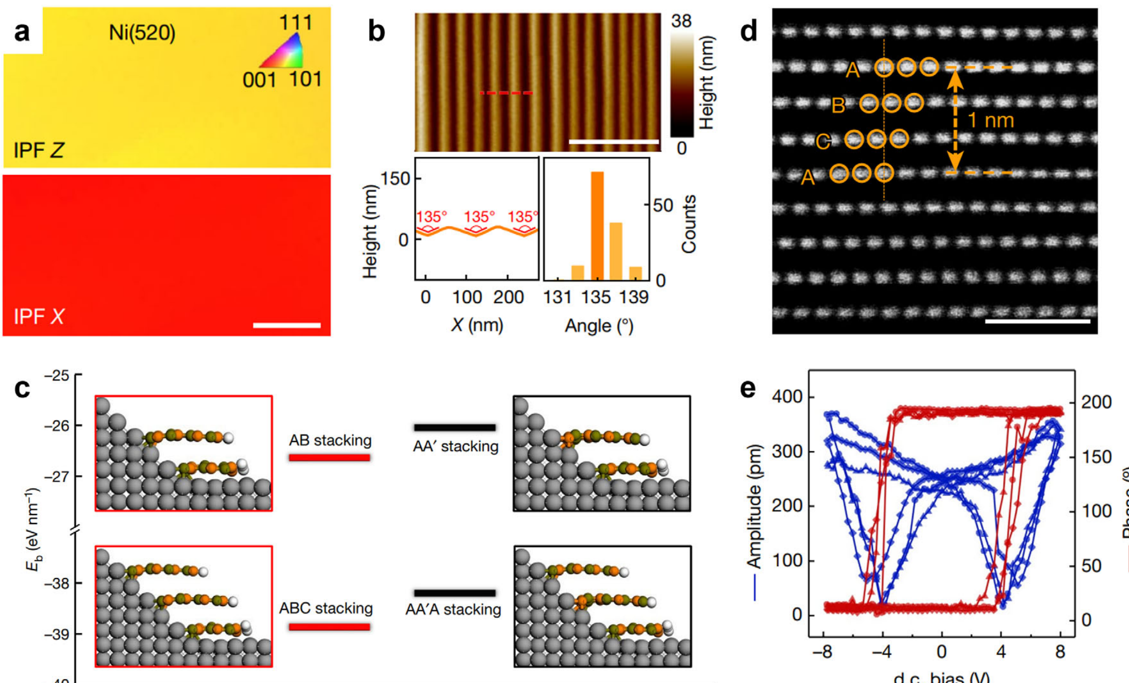

FIGURE 8 | Modulation of stacking sequence in layered BN by bevel-edge epitaxy. a) EBSD inverse pole figure of Ni(520) single crystal, showing a uniform orientation close to (111). b) AFM topography and step-orientation analysis of Ni (520), revealing periodic (100) terraces separated by ~135° (110) bevel edges. c) Calculated binding energies of different hBN stackings at the bevel edge, indicating that non-centrosymmetric AB and ABC configurations are favored over AA′-type stackings. d) Cross-sectional STEM image of multilayer rBN grown on Ni(520). e) Piezoresponse force microscopy results including amplitude and phase hysteresis loops of the rBN film, evidencing switchable out-of-plane polarization arising from the engineered stacking sequence. a–e) Reproduced with permission [57]. Copyright 2024, Springer Nature.

preference has made it difficult to realize alternative stackings such as AB or rhombohedral ABC in a uniform, wafer-scale manner. Recent work has shown that the stacking sequence can be modulated by engineering the crystallography and step structure of the underlying metal substrate [57]. When a high-index Ni(520) SC is annealed, the surface reconstructs into bunched steps consisting of wide Ni(100) terraces separated by Ni(110) bevel facets with an angle of about 135°, as revealed by orientation mapping and atomic-force microscopy (Figure 8a,b). On such a vicinal surface, density-functional calculations indicate that BN nuclei attached to the Ni(110) bevel edge are more strongly stabilized in AB and, in particular, ABC arrangements than in the conventional AA′ sequences, because the edge geometry simultaneously fixes the in-plane orientation of each BN layer and enforces a discrete lateral shift between successive layers (Figure 8c).

Experimentally, hBN grown on this stepped Ni(520) surface develops into a SC film with rhombohedral stacking, as directly visualized by cross-sectional STEM images that resolve the periodic ABC stacking sequence with an interlayer spacing of ~0.33 nm (Figure 8d). The broken inversion symmetry of this rBN film gives rise to a built-in out-of-plane polarization that can be switched by an external electric field, leading to robust interfacial ferroelectric behavior with characteristic piezoresponse amplitude and phase hysteresis loops (Figure 8e). These results demonstrate that bevel-edge epitaxy on appropriately chosen vicinal metals provides a route to stacking-engineered BN, transforming hBN from a centrosymmetric dielectric into a SC platform with intrinsic ferroelectric functionality.

However, on low-index (111) surfaces, either hBN or rBN multilayer films are selectively synthesized depending on the specific growth conditions, rather than appearing as a mixed phase (Table 2). While several studies report that the stacking order on vicinal metal (111) surfaces is determined by <110> step edges through a step-guided growth mechanism, there is currently a lack of theoretical backup data to confirm which specific stacking sequence is energetically stable at these step-edge sites. Consequently, a more profound understanding of the atomistic mechanisms governing stacking selection on (111) surfaces is still required.

5 | Integration of BN in 2D Electronics

5.1 | Advances in Transfer Methods for hBN film

Reliable exploitation of wafer-scale hBN in 2D electronics requires that as-grown films on catalytic metals be transferred onto insulating device substrates or directly onto 2D channels while preserving their structural and electronic quality via appropriately engineered wet- or dry-transfer schemes (Figure 9). Early demonstrations largely used wet chemical etching of Cu or Ni foils to release hBN in polymer-assisted transfer configurations, a straightforward approach but one that consumes the entire metal substrate and generates substantial metal-ion waste [106]. Complete dissolution of the catalyst also promotes incorporation

21967350, 0, Downloaded from https://advanced.onlinelibrary.wiley.com/doi/10.1002/admi.202501079 by Ulsan National Institute Of, Wiley Online Library on [09/04/2026]. See the Terms and Conditions (https://onlinelibrary.wiley.com/terms-and-conditions) on Wiley Online Library for rules of use; OA articles are governed by the applicable Creative Commons License

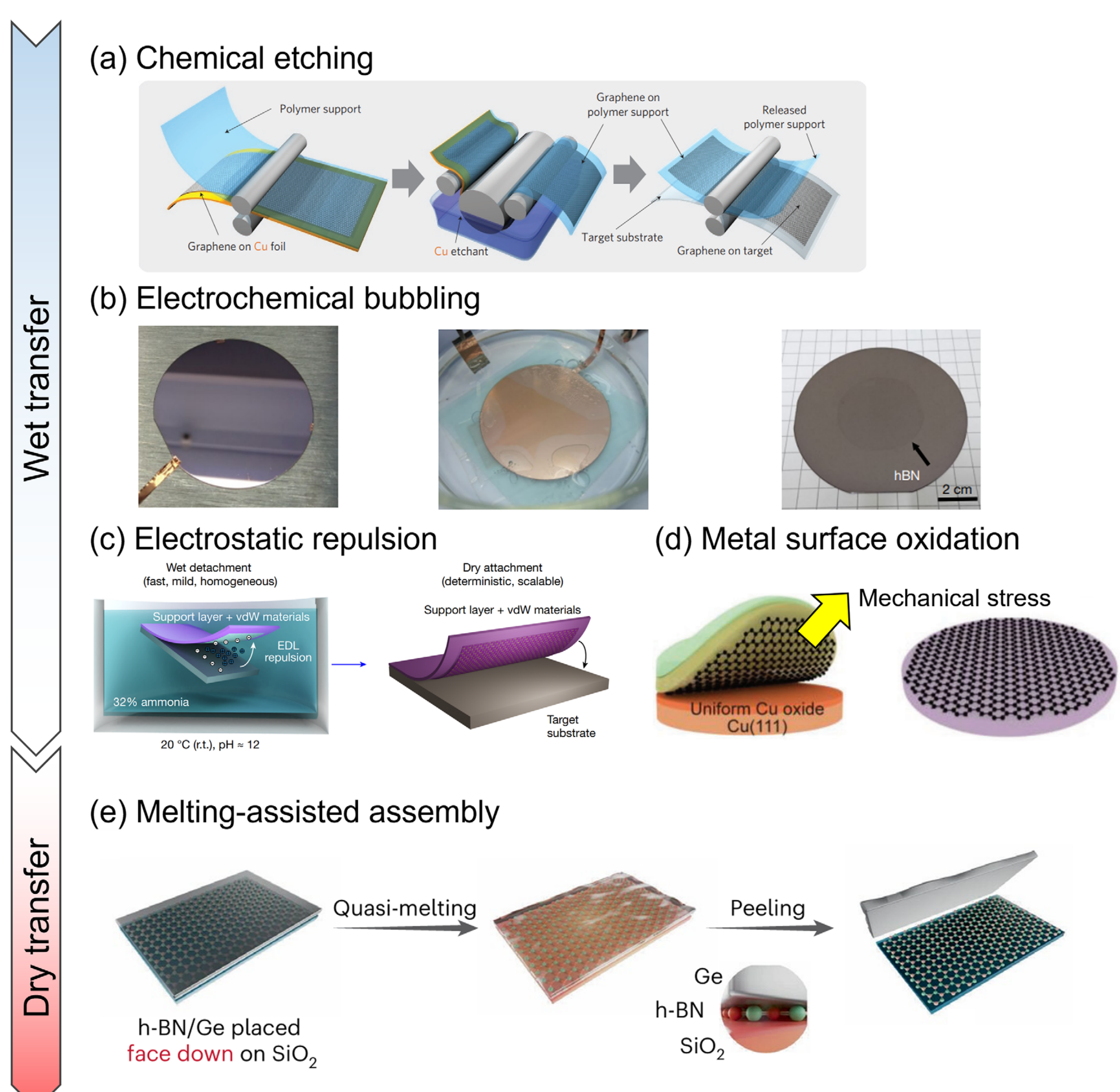

FIGURE 9 | Evolution of transfer strategies for 2D materials grown on metal substrates. Schematics and representative images summarizing the progression from conventional wet transfer to advanced dry transfer of 2D materials grown on metal foils or films: (a) polymer-assisted wet transfer via chemical etching of the metal substrate. Reproduced with permission [106]. Copyright 2010, Springer Nature; (b) electrochemical H_2-bubble–driven delamination in NaOH solution. Adapted with permission [50]. Copyright 2020, Springer Nature; (c) electrostatic-repulsion-assisted transfer using ammonia solution. Reproduced with permission [108]. Copyright 2025, Springer Nature; (d) mechanical delamination after weakening interfacial bonding by water-induced oxidation of the metal surface. Adapted with permission [109]. Copyright 2023, John Wiley and Sons; and (e) dry-transfer of hBN via the quasi-melting of Ge surface, allowing the direct peeling of 2D film onto a target substrate. Adapted with permission [110]. Copyright 2026, Springer Nature.

of etch residues and roughens the hBN surface, which degrades dielectric reliability and charge transport in subsequent devices. Electrochemical bubbling transfer, in which hydrogen evolution at the hBN/metal interface lifts off the hBN/polymer stack using NaOH or related alkaline electrolytes, reduces metal consumption and is compatible with wafer-scale delamination [50], yet introduces ionic contaminants from the electrolyte and can create macroscopic tears or wrinkles during bubble nucleation and propagation. Despite these challenges, optimized electrochemical bubbling transfer has demonstrated significant advantages over conventional wet etching by providing a more pristine interface [107]. Unlike wet transferred hBN (hBN_{wet}), which often leaves persistent metallic residues that increase surface roughness, electrochemical transferred hBN (hBN_{ele}) yields an atomically flat surface (roughness of approximately 0.19 nm) and minimizes inhomogeneous strain, as evidenced by narrower Raman 2D linewidths. Consequently, graphene transistors integrated with hBN_{ele} exhibit superior carrier mobilities—averaging over 4000 $cm^2\,V^{-1}\,s^{-1}$—whereas hBN_{wet} devices frequently underperform compared to even bare SiO_2 due to heavy particle contamination and structural defects.

To reduce such damage and contamination, recent work has explored delamination in weakly alkaline aqueous media such as ammonia solution, where electrostatic double-layer repulsion at the 2D/metal interface gradually weakens interfacial bonding,

21967350, 0, Downloaded from https://advanced.onlinelibrary.wiley.com/doi/10.1002/admi.202501079 by Ulsan National Institute Of, Wiley Online Library on [09/04/2026]. See the Terms and Conditions (https://onlinelibrary.wiley.com/terms-and-conditions) on Wiley Online Library for rules of use; OA articles are governed by the applicable Creative Commons License

enabling controlled release of hBN/metal stacks by gradually weakening interfacial bonding while largely avoiding aggressive oxidants [108]. Complementary approaches exploit mild water-induced oxidation of the metal surface to weaken its interaction with hBN, enabling purely mechanical delamination that minimizes metal and etchant residues. However, the hBN coverage makes it difficult to achieve uniform oxidation across the entire metal surface. Consequently, film tearing often occurs in non-oxidized regions, indicating that further optimization of the transfer yield is still necessary.

Most recently, a melting-assisted, polymer-free dry-transfer technique has been developed for hBN grown on Ge substrates [110]. Unlike traditional metal catalysts, the use of Ge as a semiconductor growth platform minimizes metal-induced doping and contamination. In this method, SC hBN is epitaxially grown on Ge(210) substrates and subsequently inverted onto a clean target dielectric, such as SiO_2/Si, within a vacuum chamber. By heating the Ge to a quasi-melting state (950°C), the hBN film is released from the substrate and successfully transferred to the target surface. The underlying mechanism is driven by the transition of the Ge surface into a quasi-melting state, where the surface atoms become increasingly disordered and amorphous. In this state, the binding energy between the hBN and the amorphous Ge surface significantly decreases, providing a thermodynamic pathway for the film to decouple from its growth template. Transferred graphene and hBN exhibit controlled moiré patterns depending on the stacking direction, while parallelly stacked bilayer BN displays AB-stacking, characterized by a sharp second-harmonic generation peak. These observations confirm that the method achieves an interface clean enough to investigate not only atomic flatness but also the intrinsic electronic band structures and nonlinear optical properties of 2D heterostructures. Consequently, by employing a simple rapid thermal annealing (RTA) process, the hBN film can be successfully transferred onto SiO_2/Si substrates at a wafer scale with high uniformity and minimal structural damage. These developments underscore that transfer technology is now a central part of the integration challenge for hBN-based dielectrics and highlight the need for scalable dry-transfer platforms that simultaneously minimize contamination, mechanical damage, and catalyst consumption.

5.2 | Effects of hBN Interlayer for 2D Electronic Devices

This section examines the performance enhancements achieved in 2D electronic devices by integrating large-area SC hBN into heterostructures with 2D channels, specifically focusing on how its utilization in recent synthesis studies has improved transistor characteristics (Figure 10a). For instance, in back-gated monolayer MoS_2 transistors on a 10-nm HfO_2/Si substrate, introduction of a monolayer hBN between MoS_2 and HfO_2 transforms the channel/dielectric interface [50]. When MoS_2 is placed directly on HfO_2, the room-temperature field-effect mobility is ∼2.9 cm^2 V^{-1} s^{-1} with a subthreshold swing (SS) of 111 mV dec^{-1}. Replacing the bare oxide with polycrystalline hBN increases the mobility to 6.8 cm^2 V^{-1} s^{-1}, and using wafer-scale SC hBN further enhances it to 11.8 cm^2 V^{-1} s^{-1} while reducing SS to 76 mV dec^{-1} and strongly suppressing hysteresis in the transfer curves. These trends indicate that SC hBN effectively screens charge traps and fixed charges in the underlying high-κ oxide, thereby improving both interface quality and electrostatic control.

In back-gated devices where trilayer SC hBN grown on Ni(111) is transferred onto SiO_2/Si and used as the gate dielectric underneath monolayer MoS_2, the threshold voltage shifts toward more positive values relative to bare SiO_2, consistent with reduced electron doping from the substrate and mitigation of charge trapping [51]. The room-temperature mobility of MoS_2 on trilayer hBN reaches ∼90 cm^2 V^{-1} s^{-1} compared with ∼56 cm^2 V^{-1} s^{-1} on SiO_2, reflecting weaker Coulomb scattering from interfacial impurities in the presence of the hBN spacer. These results show that even a few layers of hBN can substantially decouple 2D semiconductors from disordered oxide interfaces.

Recent work has extended this concept to hybrid high-κ/BN stacks that are transferrable at the wafer scale [28]. Ultrathin HfO_2 layers (2–10 nm) have been conformally deposited by ALD onto four-inch SC hBN/$Cu_{0.8}Ni_{0.2}$(111) wafers, forming a continuous hBN/HfO_2 composite dielectric with an equivalent oxide thickness down to 0.52 nm while maintaining a low leakage current density of 2.36×10^{-6} A cm^{-2}. After transferring onto graphene, this composite dielectric preserves the ultraflat interface (surface roughness ∼0.25 nm) and yields encapsulated graphene transistors with substantially improved statistics: the average carrier density is reduced by about a factor of six and the mobility increased by approximately threefold compared with devices encapsulated by ALD HfO_2 alone, reaching ∼10 000 cm^2 V^{-1} s^{-1} at room temperature. The top-gated transfer characteristics exhibit strong gate control with a small hysteresis window (∼40 mV), consistent with a low density of interface traps and minimal charge trapping in the dielectric stack.

Collectively, the integration of SC hBN films as an interlayer in 2D electronic devices effectively suppresses charge transfer and scattering typically induced by amorphous dielectric layers, leading to consistent performance improvements such as enhanced carrier mobility and decreased subthreshold swing. Although these studies utilize diverse synthesis substrates, transfer methods, and device architecture, they share these fundamental performance-enhancing trends. However, a significant discrepancy persists between the increasing scale of SC hBN synthesis and its practical implementation in large-scale device arrays. While achieving dimensions up to a 4-inch wafer-scale, the resulting device characterizations often remain at the single-device level. As shown in Figure 10b, statistical improvements have been demonstrated when hBN is utilized as an encapsulation layer—reaching up to 24 devices for a 10 cm growth scale—but its application as a gate interlayer in recent studies still lacks widespread device statistics. This discrepancy between material scalability and device-level demonstration undermines the claim that synthesized SC hBN can serve as a reliable and practical interlayer for scalable 2D electronics.

6 | Summary and Future Perspectives

hBN has evolved from a model system for fundamental studies into a versatile dielectric and encapsulation material for

21967350, 0, Downloaded from https://advanced.onlinelibrary.wiley.com/doi/10.1002/admi.202501079 by Ulsan National Institute Of, Wiley Online Library on [09/04/2026]. See the Terms and Conditions (https://onlinelibrary.wiley.com/terms-and-conditions) on Wiley Online Library for rules of use; OA articles are governed by the applicable Creative Commons License

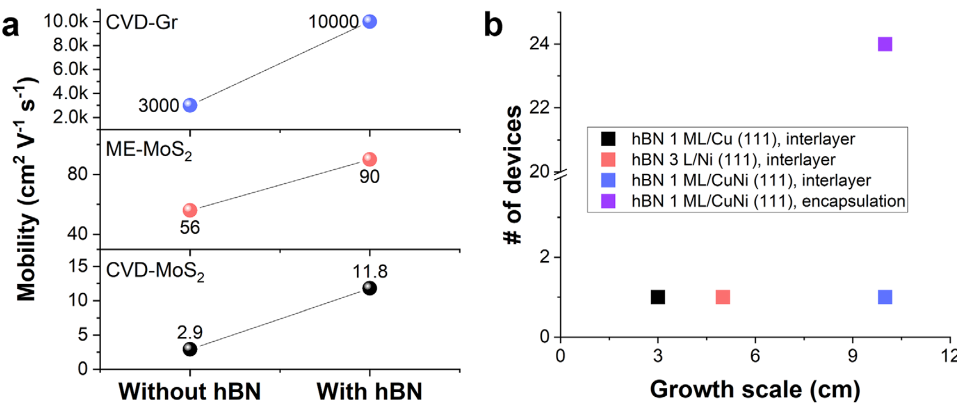

FIGURE 10 | Integration of wafer-scale hBN interlayer for 2D electronic devices. a) Mobility enhancement in various 2D channels with and without hBN films [28, 50, 51]. Mechanical exfoliation is donated as ME. b) Scalability of hBN growth and device integration [28, 50, 51]. The scatter plot shows the number of devices fabricated as a function of growth scale for different hBN synthesis methods. The scatter plot is categorized by synthesis methods and its functional roles as an interlayer and an encapsulation layer.

2D electronics. Its atomically flat, dangling-bond-free surfaces, wide bandgap, intermediate dielectric constant, and high in-plane thermal conductivity collectively enable the suppression of charged-impurity and remote-phonon scattering, a reduction of spatial potential fluctuations, and efficient lateral heat spreading.

On the synthesis side, substantial progress has been made toward scalable growth of hBN on various substrates, especially catalytic metals. SC hBN films have been achieved on metals with (111) orientations and vicinal facets through step-guided epitaxy, carefully tuned self-limiting growth windows, and most recently synchronized multilayer nucleation on Ni and Ni-based alloy substrates. Orientation control and bevel-edge epitaxy have even enabled stacking-sequence engineering, culminating in wafer-scale rhombohedral BN films with switchable out-of-plane polarization.

These materials advances have translated into tangible performance improvements in 2D devices. When used as substrates, gate dielectrics, or encapsulation layers, wafer-scale SC hBN consistently reduces charge-density inhomogeneity, suppresses hysteresis, and boosts carrier mobility in graphene, MoS_2, and related channels. Hybrid dielectrics combining hBN with ultra-thin high-κ oxides can achieve sub-nanometer equivalent oxide thickness while maintaining low leakage and high mobility. Collectively, these developments establish hBN as a key building block for advanced 2D electronics—provided its synthesis, transfer, and integration can be made fully compatible with wafer-scale manufacturing.

Despite rapid progress, several challenges remain before hBN can be widely adopted in industrial 2D electronic technologies.

1. Wafer-Scale SC Growth: The production of SC hBN at full wafer scale currently lags behind that of transition metal dichalcogenides (TMDs). While polycrystalline TMD films can now be grown on 300 mm wafers [111, 112] and SC TMDs are approaching similar dimensions [113], SC hBN growth has reached a maximum of only 4 inches, with the majority of research still confined to metal foils. To achieve the uniformity required for industrial standards, further efforts are needed to implement SC metal films on larger-scale wafers. A recent milestone demonstrated the fabrication of SC Cu(111) films on 6-inch sapphire; leveraging such platforms to include not only Cu but also Cu/Ni and pure Ni(111) will be essential for scaling the production of both monolayer and multilayer SC hBN to industrially relevant dimensions.
2. Transfer and Integration: Most high-quality hBN films are grown at temperatures incompatible with back-end-of-line processing, making a transfer step unavoidable. Present wet etching and electrochemical delamination methods allow large-area release but tend to introduce contaminants and mechanical damage. Furthermore, solvent-free mechanical force-induced dry transfer remains a formidable challenge due to the strong binding energy between catalytic metal substrates and SC hBN. Recently, a successful dry transfer of SC hBN layers grown on Ge(210) onto SiO_2/Si wafers was achieved by transitioning the Ge substrate into a quasi-melting state [110]. While this approach is currently specific to the Ge platform, the fundamental concept of promoting debonding through surface amorphization of the growth template warrants further investigation for its potential extension to conventional metal films. If successfully scaled, such a method could enable the damage-free assembly of hBN onto various insulating target substrates, providing a critical pathway for the reliable integration of wafer-scale 2D electronic components.
3. Device-Level Implementation: To date, many demonstrations have utilized wafer-grown hBN only in small numbers of devices as an interlayer. These studies primarily report simple transfer characteristics to showcase improvements in charge transport. However, such non-statistical data from a limited number of samples can lead to a distorted perception of hBN's actual impact. To rigorously evaluate the stability and reliability of the dielectric/channel interface against bias and thermal stress, it is essential to perform Bias Temperature Instability (BTI) analysis. While BTI analysis has recently been adopted for the reliability assessment of MoS_2 channels, its application to hBN-integrated systems remains scarce. Ultimately, incorporating BTI analysis is essential to

21967350, 0, Downloaded from https://advanced.onlinelibrary.wiley.com/doi/10.1002/admi.202501079 by Ulsan National Institute Of, Wiley Online Library on [09/04/2026]. See the Terms and Conditions (https://onlinelibrary.wiley.com/terms-and-conditions) on Wiley Online Library for rules of use; OA articles are governed by the applicable Creative Commons License

substantiate whether hBN interlayers offer a definitive advantage over conventional oxide dielectrics in terms of long-term operational reliability.

Overcoming these challenges—through improved wafer-scale growth, contamination-free transfer, and rigorous device benchmarking—will be critical for positioning hBN-based dielectrics and stacking-engineered BN phases as integral components of next-generation 2D electronic technologies.

Acknowledgements

This work was supported by National Research Foundation (NRF) of Korea (RS-2021-NR059677, RS-2023-00218908, RS-2024-00408180) funded by Ministry of Science and ICT, by Korea Institute for Advancement of Technology (KIAT) grant funded by the Korea Government (MOTIE) (P0023703, HRD Program for Industrial Innovation), and by the Ulsan National Institute of Science and Technology (UNIST) (1.250004.01, 1.260003.01).

Conflicts of Interest

The authors declare no conflicts of interest.

Data Availability Statement

The authors have nothing to report.

References

1. C. R. Dean, A. F. Young, I. Meric, et al., "Boron Nitride Substrates for High-Quality Graphene Electronics," *Nature Nanotechnology* 5 (2010): 722–726, https://doi.org/10.1038/nnano.2010.172.

2. R. Decker, Y. Wang, V. W. Brar, et al., "Local Electronic Properties of Graphene on a BN Substrate via Scanning Tunneling Microscopy," *Nano Letters* 11 (2011): 2291–2295, https://doi.org/10.1021/nl2005115.

3. L. Wang, I. Meric, P. Y. Huang, et al., "One-Dimensional Electrical Contact to a Two-Dimensional Material," *Science* 342 (2013): 614–617, https://doi.org/10.1126/science.1244358.

4. G.-H. Lee, Y.-J. Yu, X. Cui, et al., "Flexible and Transparent MoS_2 Field-Effect Transistors on Hexagonal Boron Nitride-Graphene Heterostructures," *ACS Nano* 7 (2013): 7931–7936, https://doi.org/10.1021/nn402954e.

5. K. F. Mak, K. He, J. Shan, and T. F. Heinz, "Control of Valley Polarization in Monolayer MoS_2 by Optical Helicity," *Nature Nanotechnology* 7 (2012): 494–498, https://doi.org/10.1038/nnano.2012.96.

6. Y. Hoshi, T. Kuroda, M. Okada, et al., "Suppression of Exciton-Exciton Annihilation in Tungsten Disulfide Monolayers Encapsulated by Hexagonal Boron Nitrides," *Physical Review B* 95 (2017): 241403, https://doi.org/10.1103/PhysRevB.95.241403.

7. C. R. Dean, L. Wang, P. Maher, et al., "Hofstadter's Butterfly and the Fractal Quantum Hall Effect in Moiré Superlattices," *Nature* 497 (2013): 598–602, https://doi.org/10.1038/nature12186.

8. E. Wang, X. Lu, S. Ding, et al., "Gaps Induced by Inversion Symmetry Breaking and Second-Generation Dirac Cones in Graphene/Hexagonal Boron Nitride," *Nature Physics* 12 (2016): 1111–1115, https://doi.org/10.1038/nphys3856.

9. K. Watanabe, T. Taniguchi, and H. Kanda, "Direct-Bandgap Properties and Evidence for Ultraviolet Lasing of Hexagonal Boron Nitride Single Crystal," *Nature Materials* 3 (2004): 404–409, https://doi.org/10.1038/nmat1134.

10. R. T. Paine and C. K. Narula, "Synthetic Routes to Boron Nitride," *Chemical Reviews* 90 (1990): 73–91.

11. A. Pakdel, Y. Bando, and D. Golberg, "Nano Boron Nitride Flatland," *Chemical Society Reviews* 43 (2014): 934–959, https://doi.org/10.1039/c3cs60260e.

12. F. Forster, A. Molina-Sanchez, S. Engels, et al., "Dielectric Screening of the Kohn Anomaly of Graphene on Hexagonal Boron Nitride," *Physical Review B* 88 (2013): 085419, https://doi.org/10.1103/PhysRevB.88.085419.

13. N. Ma and D. Jena, "Charge Scattering and Mobility in Atomically Thin Semiconductors," *Physical Review X* 4 (2014): 011043, https://doi.org/10.1103/PhysRevX.4.011043.

14. L. H. Li, E. J. G. Santos, T. Xing, et al., "Dielectric Screening in Atomically Thin Boron Nitride Nanosheets," *Nano Letters* 15 (2015): 218–223, https://doi.org/10.1021/nl503411a.

15. Y. Y. Illarionov, G. Rzepa, M. Waltl, et al., "The Role of Charge Trapping in MoS_2/SiO_2 and MoS_2/hBN Field-Effect Transistors," *2D Materials* 3 (2016): 035004, https://doi.org/10.1088/2053-1583/3/3/035004.

16. M. K. Yamoah, W. M. Yang, E. Pop, and D. Goldhaber-Gordon, "High-Velocity Saturation in Graphene Encapsulated by Hexagonal Boron Nitride," *ACS Nano* 11 (2017): 9914–9919, https://doi.org/10.1021/acsnano.7b03878.

17. A. Raja, L. Waldecker, J. Zipfel, et al., "Dielectric Disorder in Two-Dimensional Materials," *Nature Nanotechnology* 14 (2019): 832–837, https://doi.org/10.1038/s41565-019-0520-0.

18. K. Noori, N. L. Q. Cheng, F. Y. Xuan, and S. Y. Quek, "Dielectric Screening by 2D Substrates," *2D Materials* 6 (2019): 035036, https://doi.org/10.1088/2053-1583/ab1e06.

19. J. Wu, Y. Liu, Y. Liu, et al., "Large Enhancement of Thermoelectric Performance in MoS_2/h-BN Heterostructure due to Vacancy-Induced Band Hybridization," *Proceedings of the National Academy of Sciences* 117 (2020): 13929–13936, https://doi.org/10.1073/pnas.2007495117.

20. X. Zou, C.-W. Huang, L. Wang, et al., "Dielectric Engineering of a Boron Nitride/Hafnium Oxide Heterostructure for High-Performance 2D Field Effect Transistors," *Advanced Materials* 28 (2016): 2062–2069, https://doi.org/10.1002/adma.201505205.

21. X. Cui, E.-M. Shih, L. A. Jauregui, et al., "Low-Temperature Ohmic Contact to Monolayer MoS_2 by van der Waals Bonded Co/h-BN Electrodes," *Nano Letters* 17 (2017): 4781–4786, https://doi.org/10.1021/acs.nanolett.7b01536.

22. Q. A. Vu, S. Fan, S. H. Lee, M. K. Joo, W. J. Yu, and Y. H. Lee, "Near-Zero Hysteresis and Near-Ideal Subthreshold Swing in h-BN Encapsulated Single-Layer MoS_2 Field-Effect Transistors," *2D Materials* 5 (2018): 031001, https://doi.org/10.1088/2053-1583/aab672.

23. C. Pan, C.-Y. Wang, S.-J. Liang, et al., "Reconfigurable Logic and Neuromorphic Circuits Based on Electrically Tunable Two-Dimensional Homojunctions," *Nature Electronics* 3 (2020): 383–390, https://doi.org/10.1038/s41928-020-0433-9.

24. L. Wu, A. Wang, J. Shi, et al., "Atomically Sharp Interface Enabled Ultrahigh-speed Non-Volatile Memory Devices," *Nature Nanotechnology* 16 (2021): 882–887, https://doi.org/10.1038/s41565-021-00904-5.

25. L. Liu, C. Liu, L. Jiang, et al., "Ultrafast Non-Volatile Flash Memory Based on van der Waals Heterostructures," *Nature Nanotechnology* 16 (2021): 874–881, https://doi.org/10.1038/s41565-021-00921-4.

26. S. Wang, L. Liu, L. Gan, et al., "Two-Dimensional Ferroelectric Channel Transistors Integrating Ultra-Fast Memory and Neural Computing," *Nature Communications* 12 (2021): 53, https://doi.org/10.1038/s41467-020-20257-2.

27. N. A. N. Phan, H. Noh, J. Kim, et al., "Enhanced Performance of WS_2 Field-Effect Transistor Through Mono and Bilayer h-BN Tunneling Contacts," *Small* 18 (2022): 2105753, https://doi.org/10.1002/smll.202105753.

28. Y. Wang, C. Zhao, X. Gao, et al., "Ultraflat Single-Crystal Hexagonal Boron Nitride for Wafer-Scale Integration of a 2D-Compatible High-κ Metal Gate," *Nature Materials* 23 (2024): 1495–1501, https://doi.org/10.1038/s41563-024-01968-z.

21967350, 0, Downloaded from https://advanced.onlinelibrary.wiley.com/doi/10.1002/admi.202501079 by Ulsan National Institute Of, Wiley Online Library on [09/04/2026]. See the Terms and Conditions (https://onlinelibrary.wiley.com/terms-and-conditions) on Wiley Online Library for rules of use; OA articles are governed by the applicable Creative Commons License

29. P. Chen, T. L. Atallah, Z. Lin, et al., “Approaching the Intrinsic Exciton Physics Limit in Two-Dimensional Semiconductor Diodes,” *Nature* 599 (2021): 404–410, https://doi.org/10.1038/s41586-021-03949-7.

30. P. Kumar, J. Lynch, B. Song, et al., “Light–Matter Coupling in Large-Area van der Waals Superlattices,” *Nature Nanotechnology* 17 (2022): 182–189, https://doi.org/10.1038/s41565-021-01023-x.

31. Y. Chen, Y. Wang, Z. Wang, et al., “Unipolar Barrier Photodetectors Based on van der Waals Heterostructures,” *Nature Electronics* 4 (2021): 357–363, https://doi.org/10.1038/s41928-021-00586-w.

32. S. Li, Z. Zhang, X. Chen, et al., “A High-Performance In-Memory Photodetector Realized by Charge Storage in a van der Waals MISFET,” *Advanced Materials* 34 (2022): 2107734, https://doi.org/10.1002/adma.202107734.

33. H. A. Ling, J. B. Khurgin, and A. R. Davoyan, “Atomic-Void van der Waals Channel Waveguides,” *Nano Letters* 22 (2022): 6254–6261, https://doi.org/10.1021/acs.nanolett.2c01819.

34. Y. Lu, B. Li, N. Xu, et al., “One-Atom-Thick Hexagonal Boron Nitride Co-Catalyst for Enhanced Oxygen Evolution Reactions,” *Nature Communications* 14 (2023): 6965, https://doi.org/10.1038/s41467-023-42696-3.

35. S.-H. Kim, M. Kim, I. Kristanto, et al., “Horizontal Lithium Electrodeposition on Atomically Polarized Monolayer Hexagonal Boron Nitride,” *ACS Nano* 18 (2024): 24128–24138, https://doi.org/10.1021/acsnano.4c05208.

36. S. Pace, L. Martini, D. Convertino, et al., “Synthesis of Large-Scale Monolayer 1T′-$MoTe_2$ and Its Stabilization via Scalable hBN Encapsulation,” *ACS Nano* 15 (2021): 4213–4225, https://doi.org/10.1021/acsnano.0c05936.

37. D. Lee, J. J. Lee, Y. S. Kim, et al., “Remote Modulation Doping in van der Waals Heterostructure Transistors,” *Nature Electronics* 4 (2021): 664–670, https://doi.org/10.1038/s41928-021-00641-6.

38. Y. Liu, S. Liu, Z. Wang, et al., “Low-Resistance Metal Contacts to Encapsulated Semiconductor Monolayers With Long Transfer Length,” *Nature Electronics* 5 (2022): 579–585, https://doi.org/10.1038/s41928-022-00808-9.

39. D. H. Lee, N.-H. Kim, S. Jung, et al., “hBN Encapsulation Effects on the Phonon Modes of MoS_2 With a Thickness of 1 to 10 Layers,” *Advanced Materials Interfaces* 10 (2023): 2300002, https://doi.org/10.1002/admi.202300002.

40. Y. Kobayashi and T. Makimoto, “Growth of Boron Nitride on 6H–SiC Substrate by Flow-Rate Modulation Epitaxy,” *Japanese Journal of Applied Physics* 45 (2006): 3519, https://doi.org/10.1143/Jjap.45.3519.

41. Y. Kobayashi, T. Nakamura, T. Akasaka, T. Makimoto, and N. Matsumoto, “Hexagonal Boron Nitride on Ni (111) Substrate Grown by Flow-Rate Modulation Epitaxy,” *Journal of Crystal Growth* 298 (2007): 325–327, https://doi.org/10.1016/j.jcrysgro.2006.10.034.

42. Y. Kobayashi, T. Akasaka, and T. Makimoto, “Hexagonal Boron Nitride Grown by MOVPE,” *Journal of Crystal Growth* 310 (2008): 5048–5052, https://doi.org/10.1016/j.jcrysgro.2008.07.057.

43. Y. Kobayashi, C. L. Tsai, and T. Akasaka, “Optical Band Gap of h-BN Epitaxial Film Grown on *c*-Plane Sapphire Substrate,” *Physica Status Solidi C* 7, no. 7–8 (2010): 1906–1908, https://doi.org/10.1002/pssc.200983598.

44. Y. Shi, C. Hamsen, X. Jia, et al., “Synthesis of Few-Layer Hexagonal Boron Nitride Thin Film by Chemical Vapor Deposition,” *Nano Letters* 10 (2010): 4134–4139, https://doi.org/10.1021/nl1023707.

45. A. Ismach, H. Chou, D. A. Ferrer, et al., “Toward the Controlled Synthesis of Hexagonal Boron Nitride Films,” *ACS Nano* 6 (2012): 6378–6385, https://doi.org/10.1021/nn301940k.

46. K. K. Kim, A. Hsu, X. Jia, et al., “Synthesis of Monolayer Hexagonal Boron Nitride on Cu Foil Using Chemical Vapor Deposition,” *Nano Letters* 12 (2012): 161–166, https://doi.org/10.1021/nl203249a.

47. Z. Liu, Y. Gong, W. Zhou, et al., “Ultrathin High-Temperature Oxidation-Resistant Coatings of Hexagonal Boron Nitride,” *Nature Communications* 4 (2013): 2541, https://doi.org/10.1038/ncomms3541.

48. J.-H. Park, J. C. Park, S. J. Yun, et al., “Large-Area Monolayer Hexagonal Boron Nitride on Pt Foil,” *ACS Nano* 8 (2014): 8520–8528, https://doi.org/10.1021/nn503140y.

49. L. Wang, X. Xu, L. Zhang, et al., “Epitaxial Growth of a 100-Square-Centimetre Single-Crystal Hexagonal Boron Nitride Monolayer on Copper,” *Nature* 570 (2019): 91–95, https://doi.org/10.1038/s41586-019-1226-z.

50. T.-A. Chen, C.-P. Chuu, C.-C. Tseng, et al., “Wafer-Scale Single-Crystal Hexagonal Boron Nitride Monolayers on Cu (111),” *Nature* 579 (2020): 219–223, https://doi.org/10.1038/s41586-020-2009-2.

51. K. Y. Ma, L. Zhang, S. Jin, et al., “Epitaxial Single-Crystal Hexagonal Boron Nitride Multilayers on Ni (111),” *Nature* 606 (2022): 88–93, https://doi.org/10.1038/s41586-022-04745-7.

52. J. Wang, H. Lee, J. Kim, et al., “Wafer-Scale Self-Limiting Epitaxy of Bernal-Stacked Single-Crystal Boron Nitride,” *Small* (2026): 13254, https://doi.org/10.1002/smll.202513245.

53. F. Zeng, R. Wang, W. Wei, et al., “Stamped Production of Single-Crystal Hexagonal Boron Nitride Monolayers on Various Insulating Substrates,” *Nature Communications* 14 (2023): 6421, https://doi.org/10.1038/s41467-023-42270-x.

54. H. Ko, S. H. Choi, Y. Park, et al., “Atomic Sawtooth-Like Metal Films for vdW-Layered Single-Crystal Growth,” *Nature Communications* 15 (2024): 5848, https://doi.org/10.1038/s41467-024-50184-5.

55. J. Li, A. Samad, Y. Yuan, et al., “Single-Crystal hBN Monolayers From Aligned Hexagonal Islands,” *Nature Communications* 15 (2024): 8589, https://doi.org/10.1038/s41467-024-52944-9.

56. J. S. Lee, S. H. Choi, S. J. Yun, et al., “Wafer-Scale Single-Crystal Hexagonal Boron Nitride Film via Self-Collimated Grain Formation,” *Science* 362 (2018): 817–821, https://doi.org/10.1126/science.aau2132.

57. L. Wang, J. Qi, W. Wei, et al., “Bevel-Edge Epitaxy of Ferroelectric Rhombohedral Boron Nitride Single Crystal,” *Nature* 629 (2024): 74–79, https://doi.org/10.1038/s41586-024-07286-3.

58. M. Topsakal, E. Aktürk, and S. Ciraci, “First-Principles Study of Two- and One-Dimensional Honeycomb Structures of Boron Nitride,” *Physical Review B* 79 (2009): 115442, https://doi.org/10.1103/PhysRevB.79.115442.

59. R. M. Ribeiro and N. M. Peres, “Stability of Boron Nitride Bilayers: Ground-State Energies, Interlayer Distances, and Tight-Binding Description,” *Physical Review B—Condensed Matter and Materials Physics* 83 (2011): 235312, https://doi.org/10.1103/PhysRevB.83.235312.

60. D. Wickramaratne, L. Weston, and C. G. Van de Walle, “Monolayer to Bulk Properties of Hexagonal Boron Nitride,” *The Journal of Physical Chemistry C* 122 (2018): 25524–25529, https://doi.org/10.1021/acs.jpcc.8b09087.

61. J. L. Tang, J. Z. Zheng, X. H. Song, L. Cheng, and R. Q. Guo, “In-Plane Thermal Conductivity of Hexagonal Boron Nitride From 2D to 3D,” *Journal of Applied Physics* 135 (2024): 205105, https://doi.org/10.1063/5.0206028.

62. J. Iwanski, K. P. Korona, M. Tokarczyk, et al., “Revealing Polytypism in 2D Boron Nitride With UV Photoluminescence,” *NPJ 2D Materials and Applications* 8 (2024): 72, https://doi.org/10.1038/s41699-024-00511-7.

63. K. Yasuda, E. Zalys-Geller, X. Wang, et al., “Ultrafast High-Endurance Memory Based on Sliding Ferroelectrics,” *Science* 385 (2024): 53–56, https://doi.org/10.1126/science.adp3575.

64. S. Du, W. Yang, H. Gao, et al., “Sliding Memristor in Parallel-Stacked Hexagonal Boron Nitride,” *Advanced Materials* 36 (2024): 2404177, https://doi.org/10.1002/adma.202404177.

65. S.-S. Wong, Z.-Y. Lin, S.-Z. Ho, et al., “Epitaxial Ferroelectric Hexagonal Boron Nitride Grown on Graphene,” *Advanced Materials* 37 (2025): 2414442, https://doi.org/10.1002/adma.202414442.

21967350, 0, Downloaded from https://advanced.onlinelibrary.wiley.com/doi/10.1002/admi.202501079 by Ulsan National Institute Of, Wiley Online Library on [09/04/2026]. See the Terms and Conditions (https://onlinelibrary.wiley.com/terms-and-conditions) on Wiley Online Library for rules of use; OA articles are governed by the applicable Creative Commons License

66. M. Cho, B. Datta, K. Han, et al., “Moiré Exciton Polaron Engineering via Twisted hBN,” *Nano Letters* 25 (2024): 1381–1388, https://doi.org/10.1021/acs.nanolett.4c04996.

67. K. Kaasbjerg, K. S. Thygesen, and K. W. Jacobsen, “Phonon-Limited Mobility in n-Type Single-Layer MoS_2 From First Principles,” *Physical Review B* 85 (2012): 115317, https://doi.org/10.1103/PhysRevB.85.115317.

68. A. Chernikov, T. C. Berkelbach, H. M. Hill, et al., “Exciton Binding Energy and Nonhydrogenic Rydberg Series in Monolayer WS_2,” *Physical Review Letters* 113 (2014): 076802, https://doi.org/10.1103/PhysRevLett.113.076802.

69. A. Konar, T. Fang, and D. Jena, “Effect of High-κ Gate Dielectrics on Charge Transport in Graphene-Based Field Effect Transistors,” *Physical Review B* 82 (2010): 115452, https://doi.org/10.1103/PhysRevB.82.115452.

70. V. Perebeinos and P. Avouris, “Inelastic Scattering and Current Saturation in Graphene,” *Physical Review B* 81 (2010): 195442, https://doi.org/10.1103/PhysRevB.81.195442.

71. J. McPherson, J. Kim, A. Shanware, H. Mogul, and J. Rodriguez, “Proposed Universal Relationship Between Dielectric Breakdown and Dielectric Constant,” in *Digest. International Electron Devices Meeting* (IEEE, 2002): 633–636, https://doi.org/10.1109/IEDM.2002.1175919.

72. J. Robertson, “High Dielectric Constant Oxides,” *The European Physical Journal Applied Physics* 28 (2004): 265–291, https://doi.org/10.1051/epjap:2004206.

73. Y. Y. Illarionov, A. G. Banshchikov, D. K. Polyushkin, et al., “Ultrathin Calcium Fluoride Insulators for Two-Dimensional Field-Effect Transistors,” *Nature Electronics* 2 (2019): 230–235, https://doi.org/10.1038/s41928-019-0256-8.

74. K. Meng, Z. Li, P. Chen, et al., “Superionic Fluoride Gate Dielectrics With Low Diffusion Barrier for Two-Dimensional Electronics,” *Nature Nanotechnology* 19 (2024): 932–940, https://doi.org/10.1038/s41565-024-01675-5.

75. K. Liu, B. Jin, W. Han, et al., “A Wafer-Scale van der Waals Dielectric Made From an Inorganic Molecular Crystal Film,” *Nature Electronics* 4 (2021): 906–913, https://doi.org/10.1038/s41928-021-00683-w.

76. T. Knobloch, Y. Y. Illarionov, F. Ducry, et al., “The Performance Limits of Hexagonal Boron Nitride as an Insulator for Scaled CMOS Devices Based on Two-Dimensional Materials,” *Nature Electronics* 4 (2021): 98–108, https://doi.org/10.1038/s41928-020-00529-x.

77. C. Zhang, T. Tu, J. Wang, et al., “Single-Crystalline van der Waals Layered Dielectric With High Dielectric Constant,” *Nature Materials* 22 (2023): 832–837, https://doi.org/10.1038/s41563-023-01502-7.

78. L. Britnell, R. V. Gorbachev, R. Jalil, et al., “Electron Tunneling Through Ultrathin Boron Nitride Crystalline Barriers,” *Nano Letters* 12 (2012): 1707–1710, https://doi.org/10.1021/nl3002205.

79. J. Liao, Y. Zhao, X. Chen, et al., “Dielectric-Assisted Transfer Using Single-Crystal Antimony Oxide for Two-Dimensional Material Devices,” *Nature Electronics* 8 (2025): 309–321, https://doi.org/10.1038/s41928-025-01353-x.

80. D. Zeng, Z. Zhang, Z. Xue, et al., “Single-Crystalline Metal-Oxide Dielectrics for Top-Gate 2D Transistors,” *Nature* 632 (2024): 788–794, https://doi.org/10.1038/s41586-024-07786-2.

81. W. Li, J. Zhou, S. Cai, et al., “Uniform and Ultrathin High-κ Gate Dielectrics for Two-Dimensional Electronic Devices,” *Nature Electronics* 2 (2019): 563–571, https://doi.org/10.1038/s41928-019-0334-y.

82. J.-K. Huang, Y. Wan, J. Shi, et al., “High-κ Perovskite Membranes as Insulators for Two-Dimensional Transistors,” *Nature* 605 (2022): 262–267, https://doi.org/10.1038/s41586-022-04588-2.

83. S. Zhang, T. Zhang, H. Yu, et al., “Wafer-Scale High-κ HfO_2 Dielectric Films With Sub-5-Å Equivalent Oxide Thickness for 2D MoS_2 Transistors,” *Nature Communications* 17 (2026): 1888, https://doi.org/10.1038/s41467-026-68584-0.

84. Y. Xu, T. Liu, K. Liu, et al., “Scalable Integration of Hybrid High-κ Dielectric Materials on Two-Dimensional Semiconductors,” *Nature Materials* 22 (2023): 1078–1084, https://doi.org/10.1038/s41563-023-01626-w.

85. Y. Zhang, J. Yu, R. Zhu, et al., “A Single-Crystalline Native Dielectric for Two-Dimensional Semiconductors With an Equivalent Oxide Thickness Below 0.5 nm,” *Nature Electronics* 5 (2022): 643–649, https://doi.org/10.1038/s41928-022-00824-9.

86. J. Shao, Y. Zhu, J. Liao, et al., “Texture-Engineered Fabrication of Ultraflat, 6-Inch Single-Crystal Cu(111) Wafers,” *Science Advances* 11 (2025): ady1943, https://doi.org/10.1126/sciadv.ady1943.

87. M. Seol, M.-H. Lee, H. Kim, et al., “High-Throughput Growth of Wafer-Scale Monolayer Transition Metal Dichalcogenide via Vertical Ostwald Ripening,” *Advanced Materials* 32 (2020): 2003542, https://doi.org/10.1002/adma.202003542.

88. J. Zhu, J.-H. Park, S. A. Vitale, et al., “Low-Thermal-Budget Synthesis of Monolayer Molybdenum Disulfide for Silicon Back-End-of-Line Integration on a 200 mm Platform,” *Nature Nanotechnology* 18 (2023): 456–463, https://doi.org/10.1038/s41565-023-01375-6.

89. Y. Xia, X. Chen, J. Wei, et al., “12-Inch Growth of Uniform MoS_2 Monolayer for Integrated Circuit Manufacture,” *Nature Materials* 22 (2023): 1324–1331, https://doi.org/10.1038/s41563-023-01671-5.

90. Y. Kobayashi and T. Akasaka, “Hexagonal BN Epitaxial Growth on (0 0 0 1) Sapphire Substrate by MOVPE,” *Journal of Crystal Growth* 310 (2008): 5044–5047, https://doi.org/10.1016/j.jcrysgro.2008.07.010.

91. G. Kim, A.-R. Jang, H. Y. Jeong, Z. Lee, D. J. Kang, and H. S. Shin, “Growth of High-Crystalline, Single-Layer Hexagonal Boron Nitride on Recyclable Platinum Foil,” *Nano Letters* 13 (2013): 1834–1839, https://doi.org/10.1021/nl400559s.

92. A.-R. Jang, S. Hong, C. Hyun, et al., “Wafer-Scale and Wrinkle-Free Epitaxial Growth of Single-Orientated Multilayer Hexagonal Boron Nitride on Sapphire,” *Nano Letters* 16 (2016): 3360–3366, https://doi.org/10.1021/acs.nanolett.6b01051.

93. A. Bansal, M. Hilse, B. Huet, et al., “Substrate Modification During Chemical Vapor Deposition of hBN on Sapphire,” *ACS Applied Materials & Interfaces* 13 (2021): 54516–54526, https://doi.org/10.1021/acsami.1c14591.

94. L. Chen, Z. Long, J. Liu, et al., “Polarization Sensitive Vacuum-Ultraviolet Photodetectors Based on m -Plane h-BN,” *Advanced Materials* 37 (2025): 2503846, https://doi.org/10.1002/adma.202503846.

95. J. Meng, X. Zhang, Y. Wang, et al., “Aligned Growth of Millimeter-Size Hexagonal Boron Nitride Single-Crystal Domains on Epitaxial Nickel Thin Film,” *Small* 13 (2017): 1604179, https://doi.org/10.1002/smll.201604179.

96. S. M. Kim, A. Hsu, M. H. Park, et al., “Synthesis of Large-Area Multilayer Hexagonal Boron Nitride for High Material Performance,” *Nature Communications* 6 (2015): 8662, https://doi.org/10.1038/ncomms9662.

97. J. Qi, C. Ma, Q. Guo, et al., “Stacking-Controlled Growth of rBN Crystalline Films With High Nonlinear Optical Conversion Efficiency up to 1%,” *Advanced Materials* 36 (2024): 2303122, https://doi.org/10.1002/adma.202303122.

98. H. Shi, M. Wang, H. Chen, et al., “Layer-by-Layer Connection for Large Area Single Crystal Boron Nitride Multilayer Films,” *ACS Applied Materials & Interfaces* 17 (2025): 14660–14669, https://doi.org/10.1021/acsami.4c19877.

99. Y. Uchida, S. Nakandakari, K. Kawahara, S. Yamasaki, M. Mitsuhara, and H. Ago, “Controlled Growth of Large-Area Uniform Multilayer Hexagonal Boron Nitride as an Effective 2D Substrate,” *ACS Nano* 12 (2018): 6236–6244, https://doi.org/10.1021/acsnano.8b03055.

100. S. K. Jang, J. Youn, Y. J. Song, and S. Lee, “Synthesis and Characterization of Hexagonal Boron Nitride as a Gate Dielectric,” *Scientific Reports* 6 (2016): 30449, https://doi.org/10.1038/srep30449.

21967350, 0, Downloaded from https://advanced.onlinelibrary.wiley.com/doi/10.1002/admi.202501079 by Ulsan National Institute Of, Wiley Online Library on [09/04/2026]. See the Terms and Conditions (https://onlinelibrary.wiley.com/terms-and-conditions) on Wiley Online Library for rules of use; OA articles are governed by the applicable Creative Commons License

101. S. Caneva, R. S. Weatherup, B. C. Bayer, et al., "Controlling Catalyst Bulk Reservoir Effects for Monolayer Hexagonal Boron Nitride CVD," *Nano Letters* 16 (2016): 1250–1261, https://doi.org/10.1021/acs.nanolett.5b04586.

102. A. Rice, A. Allerman, M. Crawford, et al., "Effects of Deposition Temperature and Ammonia Flow on Metal-Organic Chemical Vapor Deposition of Hexagonal Boron Nitride," *Journal of Crystal Growth* 485 (2018): 90–95, https://doi.org/10.1016/j.jcrysgro.2017.12.011.

103. C. Liu, T. Liu, Z. Zhang, et al., "Understanding Epitaxial Growth of Two-Dimensional Materials and Their Homostructures," *Nature Nanotechnology* 19 (2024): 907–918, https://doi.org/10.1038/s41565-024-01704-3.

104. J. C. Dong, L. N. Zhang, X. Y. Dai, and F. Ding, "The Epitaxy of 2D Materials Growth," *Nature Communications* 11 (2020): 5862, https://doi.org/10.1038/s41467-020-19752-3.

105. L. N. Zhang, X. Kong, J. C. Dong, and F. Ding, "A Mechanism for Thickness-Controllable Single Crystalline 2D Materials Growth," *Science Bulletin* 68 (2023): 2936–2944, https://doi.org/10.1016/j.scib.2023.10.037.

106. S. Bae, H. Kim, Y. Lee, et al., "Roll-to-Roll Production of 30-Inch Graphene Films for Transparent Electrodes," *Nature Nanotechnology* 5 (2010): 574–578, https://doi.org/10.1038/nnano.2010.132.

107. S. Fukamachi, P. Solís-Fernández, K. Kawahara, et al., "Large-Area Synthesis and Transfer of Multilayer Hexagonal Boron Nitride for Enhanced Graphene Device Arrays," *Nature Electronics* 6 (2023): 126–136, https://doi.org/10.1038/s41928-022-00911-x.

108. X. Zheng, J. Wang, J. Jiang, et al., "Electrostatic-Repulsion-Based Transfer of van der Waals Materials," *Nature* 645 (2025): 906–914, https://doi.org/10.1038/s41586-025-09510-0.

109. Z. Hu, F. Li, H. Wu, et al., "Rapid and Scalable Transfer of Large-Area Graphene Wafers," *Advanced Materials* 35 (2023): 2300621, https://doi.org/10.1002/adma.202300621.

110. C. Zhang, Q. Xie, C. Jiang, et al., "Melting-Assisted Assembly of Twisted Graphene/h-BN Superlattices With Clean Interfaces," *Nature Synthesis* (2026): 1–9, https://doi.org/10.1038/s44160-026-01000-z.

111. K. Maxey, C. Naylor, K. O'Brien, et al., "300 mm MOCVD 2D CMOS Materials for More (Than) Moore Scaling, " in *2022 IEEE Symposium on VLSI Technology and Circuits* (VLSI Technology and Circuits) (IEEE, 2022): 419–420, https://doi.org/10.1109/VLSITechnologyandCir46769.2022.9830457.

112. C. Dorow, T. Schram, Q. Smets, et al., "Exploring Manufacturability of Novel 2D Channel Materials: 300 Mm Wafer-Scale 2D NMOS & PMOS Using MoS_2, WS_2, & WSe_2," in 2023 International Electron Devices Meeting (IEDM) (IEEE, 2023): 1–4, https://doi.org/10.1109/IEDM45741.2023.10413874.

113. X. Zou, Y. Zhao, D. Fan, et al., "Robust Epitaxy of Single-Crystal Transition-Metal Dichalcogenides on Lanthanum-Passivated Sapphire," *Science* 390 (2025): aea0849, https://doi.org/10.1126/science.aea0849.

21967350, 0, Downloaded from https://advanced.onlinelibrary.wiley.com/doi/10.1002/admi.202501079 by Ulsan National Institute Of, Wiley Online Library on [09/04/2026]. See the Terms and Conditions (https://onlinelibrary.wiley.com/terms-and-conditions) on Wiley Online Library for rules of use; OA articles are governed by the applicable Creative Commons License